AGU PUBLICATIONS

JGR

Journal of Geophysical Research: Solid Earth

RESEARCH ARTICLE
10.1002/2013JB010521

Key Points:
- Andesites from Volcán de Colima are microstructurally complex
- Their microstructural complexity influences their properties
- Micromechanical modeling is therefore a challenge

Correspondence to:
M. J. Heap,
heap@unistra.fr

Citation:
Heap, M. J., Y. Lavallée, L. Petrakova, P. Baud, T. Reuschlé, N. R. Varley, and D. B. Dingwell (2014), Microstructural controls on the physical and mechanical properties of edifice-forming andesites at Volcán de Colima, Mexico, *J. Geophys. Res. Solid Earth*, *119*, 2925–2963, doi:10.1002/2013JB010521.

Received 17 JUL 2013
Accepted 26 MAR 2014
Accepted article online 29 MAR 2014
Published online 23 APR 2014

Microstructural controls on the physical and mechanical properties of edifice-forming andesites at Volcán de Colima, Mexico

M. J. Heap[1], Y. Lavallée[2], L. Petrakova[3], P. Baud[1], T. Reuschlé[1], N. R. Varley[4], and D. B. Dingwell[3]

[1]Laboratoire de Déformation des Roches, Équipe de Géophysique Expérimentale, Institut de Physique de Globe de Strasbourg (UMR 7516 CNRS, Université de Strasbourg/EOST), Strasbourg, France, [2]School of Environmental Sciences, University of Liverpool, Liverpool, UK, [3]Earth and Environment, University of Munich, München, Germany, [4]Facultad de Ciencias, Universidad de Colima, Colima, Mexico

Abstract The reliable assessment of volcanic unrest must rest on an understanding of the rocks that form the edifice. It is their microstructure that dictates their physical properties and mechanical behavior and thus the response of the edifice to stress perturbations during unrest. We evaluate the interplay between microstructure and rock properties for a suite of edifice-forming rocks from Volcán de Colima (Mexico). Microstructural analyses expose (1) a pervasive, isotropic microcrack network, (2) a high, subspherical vesicle density, and (3) a wide vesicle size distribution. This complex microstructure severely impacts their physical and mechanical properties. In detail, porosities are high and range from 8 to 29%. As a consequence, elastic wave velocities, Youngs moduli, and uniaxial compressive strengths are low, and permeabilities are high. All of the rock properties demonstrate a wide range. For example, strength decreases by a factor of 8 and permeability increases by 4 orders of magnitude over the porosity range. Below a porosity of 11–14%, the permeability-porosity trend follows a power law with a much higher exponent. Microstructurally, this represents a critical vesicle content that efficiently connects the microcrack population and permits a much more direct path through the sample, rather than restricting flow to long and tortuous microcracks. Values of tortuosity inferred from the Kozeny-Carman permeability model support this hypothesis. However, we find that the complex microstructure precludes a complete description of their mechanical behavior through micromechanical modeling. We urge that the findings of this study be considered in volcanic hazard assessments at andesitic stratovolcanoes.

1. Introduction

A comprehensive description of the microstructural, physical, and mechanical properties of edifice-forming rocks represents essential input for the development of effective and robust volcanic unrest models [e.g., *Sparks*, 2003]. In the assessment of the response of a volcanic edifice to the stress perturbations likely to accompany any unrest activity, details of the response of the rocks become central to the question of ascribing the permissible mechanistic sources behind geophysical, geodetic, and geochemical signals of unrest [e.g., *Gottsmann et al.*, 2011]. An improved understanding of the relationships between rock microstructure (e.g., microcracks and vesicles), rock physical properties (e.g., porosity, bulk density, elastic wave velocities, and permeability), and rock mechanical properties (e.g., strength) of representative materials should therefore allow us to (1) improve the imaging of subsurface activity [e.g., *Manconi et al.*, 2007], (2) construct a better scheme to assess the structural stability of the volcano [e.g., *Voight*, 2000; *Gudmundsson*, 2011], and (3) better understand the role of the host rocks in dictating eruption characteristics and progression [e.g., *Jaupart*, 1998; *Costa et al.*, 2009].

Volcanic structures are haphazardly assembled from the products of successive effusive and explosive eruptions. The rapid and heterogeneous construction, in both time and space, of volcanic edifices renders them inherently unstable [e.g., *McGuire*, 1996]. During this rapid construction, volcanic rocks are subjected to variable but rapid solidification due to the temperature changes associated with their eruptive and emplacement history. In this process, disequilibrium crystallization, gas exsolution, degassing, sintering/welding, and partial vitrification/devitrification contribute to generate a wide range of volcanic materials. Complex variations in temperature, stress, strain, and strain rate during magma ascent may further promote the development of additional microstructural and macrostructural features (e.g., microcracks and flow bands), both in the eruptive products and in the host rock. As a result, volcanic structures are generally made

up of many layers that harbor very different microstructural, physical, and mechanical properties [e.g., *Gudmundsson*, 2011]. To emphasize, the porosity of volcanic rocks can vary from essentially zero up to 97% in the case of reticulite. Experimental rock deformation has been dominated by studies of homogeneous sedimentary and intrusive igneous rocks [see *Paterson and Wong*, 2005]. Only recently have studies begun to investigate the microstructural, physical, and mechanical properties of volcanic rocks [e.g., *Rocchi et al.*, 2004; *Balme et al.*, 2004; *Vinciguerra et al.*, 2005; *Stanchits et al.*, 2006; *Jeong et al.*, 2007; *Benson et al.*, 2008; *Smith et al.*, 2009; *Fortin et al.*, 2011; *Heap et al.*, 2011; *Zhu et al.*, 2011; *Loaiza et al.*, 2012; *Adelinet et al.*, 2013]. Though few in number, these studies have already exposed a wide range of physical properties and mechanical behavior owing to a wide variety of microstructure.

In this study, we evaluate the microstructure (i.e., microcrack density and anisotropy, and vesicle density, shape, and size distribution) and the physical (i.e., porosity, dynamic and static elastic moduli, elastic wave velocities and anisotropy, and permeability) and mechanical properties (i.e., strength) of a representative suite of andesitic rocks from the active Volcán de Colima, Mexico. The focus of this study is to characterize edifice host rocks; the host rock will very rarely exceed its glass transition temperature (740°C) [*Lavallée et al.*, 2012], and therefore the room temperature experiments reported in this study should correspond closely to the state of the rocks comprising the edifice. We then explore the adequacy of micromechanical models (pore-emanated crack and sliding wing-crack modeling) in an attempt to decipher their mechanical behavior and geometrical permeability modeling (Kozeny-Carman) to understand the physics underpinning fluid transport. With the aim of a better understanding of volcanically active provinces, we complement our data with an assessment of the impact of temperatures representative of conduit margins (450°C) on the microstructural, physical, and mechanical properties of the andesites. Thermal microcracks form as a result of the buildup of internal stresses due to the following: (1) the thermal expansion mismatch between the different phases present in the material, (2) thermal expansion anisotropy within individual minerals, and (3) thermal gradients [e.g., *Richter and Simmons*, 1974; *Yong and Wang*, 1980]. Thermal microcracking has been previously shown to induce changes to the physical properties of rocks [e.g., *David et al.*, 1999]. However, few studies have investigated the propensity of volcanic rocks to develop thermal microcracks and their consequences on rock physical properties. In a volcanic setting, thermal microcracking of the conduit wall rock and the surrounding country rock could have consequences on the progression of the eruption [e.g., *Costa et al.*, 2009], and, importantly, on the stability of the volcanic edifice as a whole [e.g., *Donnadieu et al.*, 2001; *Gudmundsson*, 2011]. Finally, we discuss some implications of our findings for andesitic stratovolcanoes.

2. Case Study: Volcán de Colima (Mexico)

Volcán de Colima (Mexico, 19°30′N, 103°37′W, Figure 1) is a persistently active and frequently collapsing volcano located at the western end of the Trans-Mexican Volcanic Belt. Locally, the stratovolcano marks the intersection between the N-S trending Colima Rift Zone and the NE-SW trending Tamazula Fault [*Norini et al.*, 2010]. The volcanic complex comprises the older, extinct edifice of Nevado de Colima and the active ($<$50 ka) Fuego de Colima, constructed in the amphitheater of an earlier collapse structure (Figure 1). At least five collapse events during the last 18,500 years have occurred with widely distributed debris avalanche deposits found to the south [*Cortés et al.*, 2010], the most recent being 2550 B.P.

Recent eruptive activity at Volcán de Colima has been described as occurring in cycles with an interval of approximately 100 years [*Luhr*, 2002]. The last two cycles of which ended in 1818 and 1913 with volcanic explosivity index four explosive eruptions (between larger Plinian or sub-Plinian eruptions). Typical activity is characterized by episodes of both effusive and Vulcanian explosive events. Multifaceted transitions between styles of activity point to a complex plumbing system with multiple pathways [*Lavallée et al.*, 2012] and various magma reservoirs located at different depths. Studies of melt inclusions have defined a range of crystallization depths based upon the entrapment pressure of both dissolved H_2O and CO_2 for the 1998–2005 period [*Reubi et al.*, 2013]. The majority indicate depths less than 4 km, matching depths for volcano-tectonic seismicity recorded as precursors to the 1998–1999 eruption [*Zobin et al.*, 2002a].

The most recent eruption commenced in January 2013 with Vulcanian explosions and the emplacement of a new lava dome and flow and is ongoing as of February 2014. The previous prolonged episode lasted from November 1998 until June 2011. During this period, there were five episodes of dome growth, of varying duration and effusion rate, from 2.5 months and 8 $m^3 s^{-1}$ in 2004 [*Varley et al.*, 2010] to the excessively low rate of 0.02 $m^3 s^{-1}$ for

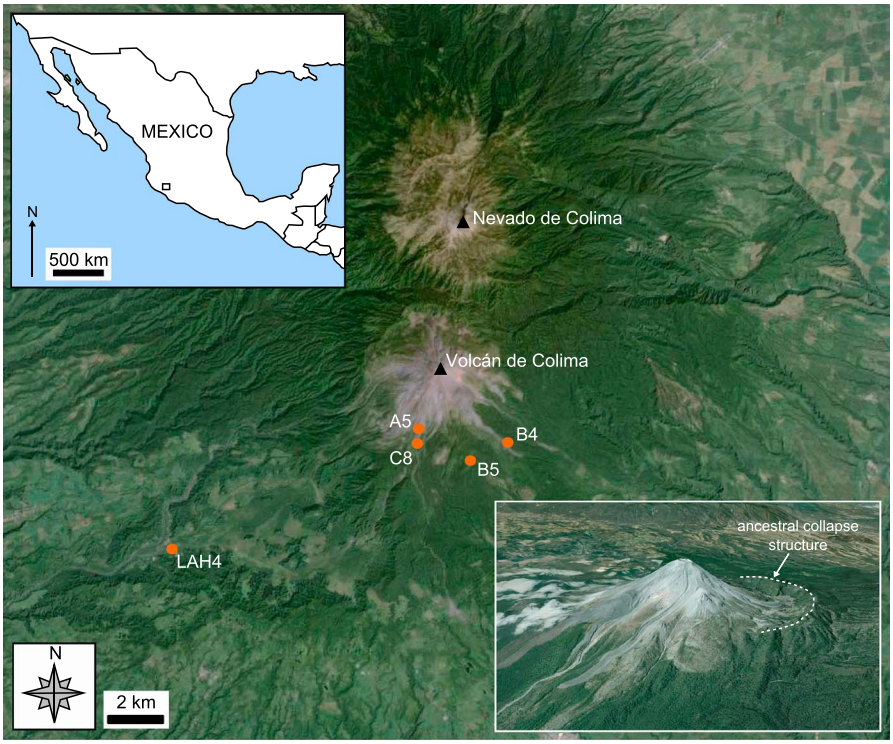

Figure 1. A Google Earth™ map showing the locations of the sampling sites with respect to Volcán de Colima. Insets show a map of Mexico (the rectangular box corresponds to the position of the locality map) and a Google Earth™ image of Volcán de Colima showing the ancestral collapse structure (dashed white line).

the final episode, which lasted 4.5 years. Slow protracted dome growth occurred in 2001–2003 and 2007–2011, while fast episodes, more typical for this type of volcano, were witnessed in 1998–1999, 2004, and 2005, the former two extending to form substantial lava flows. Two types of explosive activity have also characterized the recent eruption: larger Vulcanian events that have often destroyed a previously emplaced dome and small events of variable ash contents, which have been generated with a repose period of the order of a few hours. The most intense period of activity occurred in 2005 during which at least 30 larger explosions produced pyroclastic flows, reaching 5.4 km to the SE of the volcano [*Varley et al.*, 2010].

Recent eruptive activity has been extensively monitored by seismicity [*Arámbula-Mendoza et al.*, 2011], with also gas geochemistry [*Taran et al.*, 2002; *Varley and Taran*, 2003], infrared imaging [*Hutchinson et al.*, 2013; *Stevenson and Varley*, 2008], and deformation [*Zobin et al.*, 2002b]. The local population has increased since the 1913 Plinian eruption whose impact was relatively minimal [*Saucedo et al.*, 2010]. The increased vulnerability has been highlighted by the impact of lahars during recent years, which have shown a clear relationship with the volume of pyroclastic period deposited in the ravines [*Dávila et al.*, 2007]. Modeling collapse events has emphasized the need to understand and ideally predict the failing of lava domes [*Sulpizio et al.*, 2010] while stochastic flank collapse probability modeling has yielded two scenarios: (1) that Colima is 110 years overdue for a debris avalanche event (DAE) and (2) that this next DAE will occur 345 years from the present [*Borselli et al.*, 2011].

The magma erupts at temperatures of 960–1031°C [*Reubi and Blundy*, 2008], and the temperature of fumaroles at the surface has been measured to be 820°C in 2001 [*Varley and Taran*, 2003]. The temperature of the outer carapace of a lava dome is dependent upon its size and the effusion rate; temperatures can reach >500°C when the dome is small with exogenic growth and, when large, the temperature is dependent on the effusion rate (for fast growing domes this can be >300°C). The core of the dome remains hot, as evidenced by routine thermal imaging of internal dome structures, occasionally exposed by the partial shedding of the talus [*Mueller et al.*, 2013]. The erupted products of Volcán de Colima have varied only slightly in bulk composition during recent years, being andesitic and containing ~58–61 wt % SiO_2 [*Luhr*, 2002; *Savov et al.*, 2008]. Recent field-based studies [*Lavallée et al.*, 2012, and references therein] have revealed the porosity of eruptive products to be, in general, lower than 40%.

Table 1. Averaged X-ray Fluorescence Analysis of the Bulk Geochemical Composition of Each of the Studied Andesites

Sample	B5	B4	A5	C8	LAH4
SiO_2	59.72	60.23	58.87	61.41	59.10
Al_2O_3	16.85	17.56	17.87	17.84	17.45
Fe_2O_3	6.25	5.95	5.89	5.43	6.13
MnO	0.12	0.11	0.10	0.10	0.11
MgO	3.90	3.08	3.63	2.29	4.04
CaO	6.05	5.86	6.44	5.49	6.62
Na_2O	4.51	4.73	4.61	4.88	4.52
K_2O	1.27	1.32	1.18	1.44	1.19
TiO_2	0.60	0.60	0.60	0.55	0.62
P_2O_5	0.18	0.20	0.18	0.20	0.19
LOI	0.05	0.03	0.10	0.00	0.00
Total	99.47	99.59	99.27	99.61	99.97

3. Experimental Materials and Methods

3.1. Experimental Materials

For the purpose of our study we selected five andesitic blocks (A5, B4, B5, C8, and LAH4) to represent the variability of the material forming the volcanic edifice [*Lavallée et al.*, 2012]. A5 is from the 1998–1999 lava flow in the Cordoban ravine, B4 was taken from the 1975–1976 lava flow from the southeast slope of the volcano, B5 is from an older lava flow of unknown age, C8 was taken from the 1998–1999 blow-and-ash flow in the San Antonio ravine, and LAH4 is a block of unknown age collected from a lahar deposit on the west flank of the volcano (in the El Zarco riverbed near La Becerrera). The locations of the collection sites are indicated in Figure 1.

X-ray fluorescence analysis of the bulk geochemical composition of each andesite block is presented in Table 1 and shows that the andesites contain between 58 and 61 wt % silica (similar to the bulk chemical compositions provided by *Luhr* [2002]). Optical microscopic analysis (Figure 2a) under crossed polarized transmitted light has shown the andesites to have a porphyritic texture containing (commonly microcracked) phenocrysts ($<$1.5 mm) of plagioclase (13–25%), orthopyroxene (2–4%), and clinopyroxene (3–4%) within a microlitic groundmass (59–68%). The plagioclase crystals are commonly zoned and twinned (Figure 2a). The groundmass contains interstitial glass with a glass transition temperature of about 740°C at a rate of 10°C/min [*Lavallée et al.*, 2012]. Under reflected light (Figure 2b) and using a scanning electron microscope (SEM, Figure 2c), methods that permit a better examination of rock microstructure, we observe that the andesites are pervasively microcracked and contain many vesicles.

Numerous cylindrical core samples were prepared from each of the five blocks of andesite. Samples were cored to a diameter of 20 mm and precision ground to a nominal length of 40 mm. The collected andesite blocks were loose blocks selected from lava, block-and-ash flow, and lahar deposits (Figure 1) and are therefore unorientated with respect to any volcanological feature and with respect to each other. In this study we refer to an *X*, *Y*, and *Z* directions for each of the blocks. Our *Z* direction was chosen to maximize the number of cylindrical core samples we could take from each block; *X* and *Y* are orthogonal to this coring direction.

3.2. Experimental Methods

The methods used in this study are presented below. In each case, further details can be found in Appendix A.

3.2.1. Microstructural Characterization

Two-dimensional quantitative microcrack and vesicle analyses were performed on thin sections (in the *XY* plane) prepared from fluorescent-epoxy-impregnated samples of each andesite. Volcanic rocks are persistently exposed to a combination of thermal and mechanical stresses and, as a result, are often highly fractured. Microcrack surface area per unit volume was determined using classical stereological techniques [*Underwood*, 1970], and microcrack anisotropy was measured using the modified Cantor-dust method [*Volland and Kruhl*, 2004] included in the automated pattern quantification toolbox AMOCADO [*Gerik and Kruhl*, 2009]. Vesicles in volcanic rocks represent the solidified relicts of degassing processes in magmas. For this reason, their statistical analysis can provide information relating to the physical processes that drive magma ascent and eruption [see *Shea et al.*, 2010, and references therein]. In this study we are interested in vesicle size and shape distributions in order to evaluate the micromechanics responsible for their deformation. Vesicle area, density, circularity, aspect ratio, and roundness were determined using image processing software ImageJ.

3.2.2. Connected and Total Porosities

The connected water porosities of the samples were measured using the triple-weight water saturation (distilled water) method, using Archimedes' principal [see *Guéguen and Palciauskas*, 1994]. The powder skeletal densities required for the calculation of total porosity were measured using a helium pycnometer (AccuPyc II 1340).

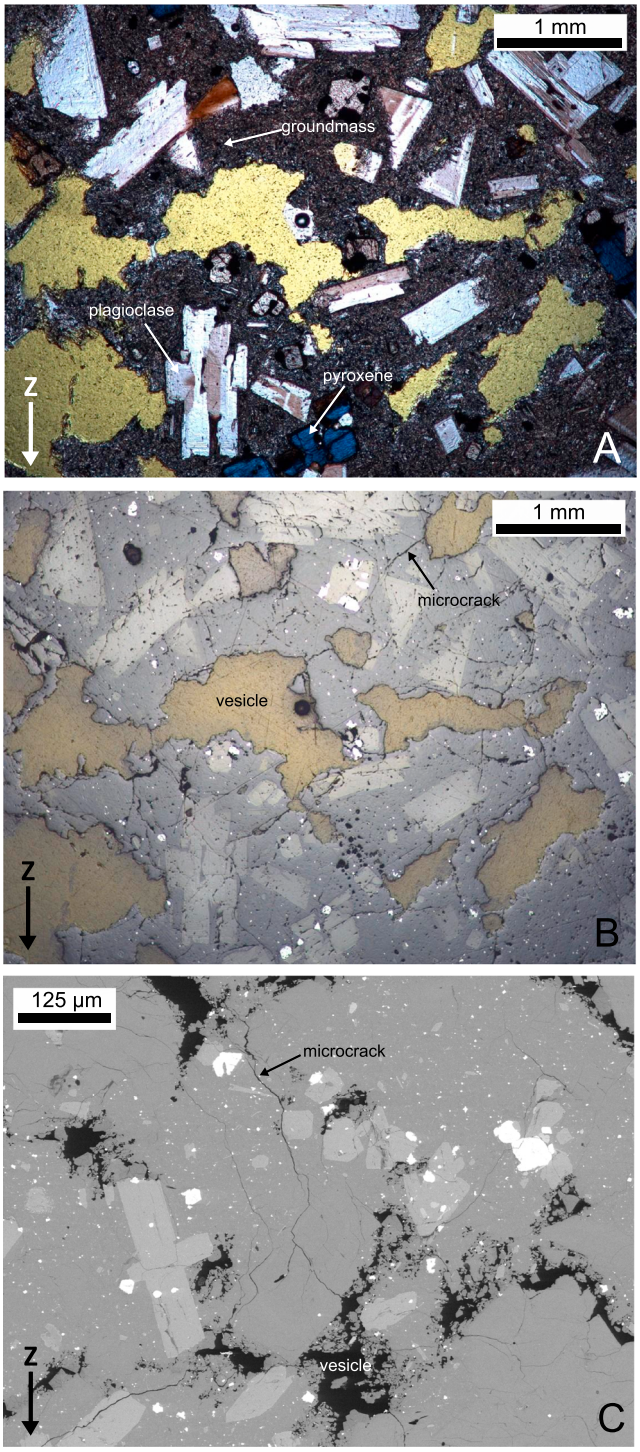

Figure 2. (a) A photomicrograph (taken under transmitted cross-polarized light) of one of the andesites investigated in this study (in this case C8). The common minerals are identified on the figure (note: the green areas are vesicles, see Figure 2b). (b) A photomicrograph (taken under reflected light) of the same area. The microstructural elements are identified on the figure. (c) Scanning electron microscope image of a sample of B5. The microstructural elements are identified on the figure.

3.2.3. Elastic Wave Velocities

P and *S* wave velocities were measured along the long axis of the cylindrical samples (i.e., the *Z* direction) under both dry conditions (i.e., the samples were dried for at least 24 h in a vacuum oven at 40°C, and then the measurements were made under ambient humidity conditions) and water-saturated (i.e., vacuum saturated with distilled water) conditions. All measurements were collected under ambient laboratory conditions and an axial stress of 1.9 MPa. To investigate the anisotropic nature of the andesites we machined cubes (approximately 50 × 50 × 50 mm) from each of the andesite blocks. *P* and *S* wave velocities could then be measured in each of the *X*, *Y*, and *Z* directions with a reduced risk of sample variability influencing the results (as may be the case if three orthogonal cores were prepared).

3.2.4. Elastic Moduli

The measured elastic wave velocities (see section 3.2.3) were subsequently used to calculate the dynamic Young's modulus E_d and the dynamic Poisson's ratio ν_d [see *Guéguen and Palciauskas*, 1994]. For the static Young's moduli E_s, we used the tangent moduli defined as the local slope of the stress-strain curves collected during the uniaxial compressive strength (UCS) experiments described in section 3.2.6. The moduli were calculated at the axial stress level corresponding to the maximum slope (typically at axial stresses between 15 and 100 MPa, depending on the sample).

3.2.5. Permeability Measurements

Water (distilled) permeability measurements were made in a hydrostatic pressure vessel along the long axis of the cylindrical samples (i.e., the *Z* direction). Permeabilities were measured for a suite of samples that best cover the observed range of connected water porosities (from 7.4 to 23.8%). Fluid volume flux was measured during steady state flow (under a confining pressure of 2 MPa), and permeability was calculated using

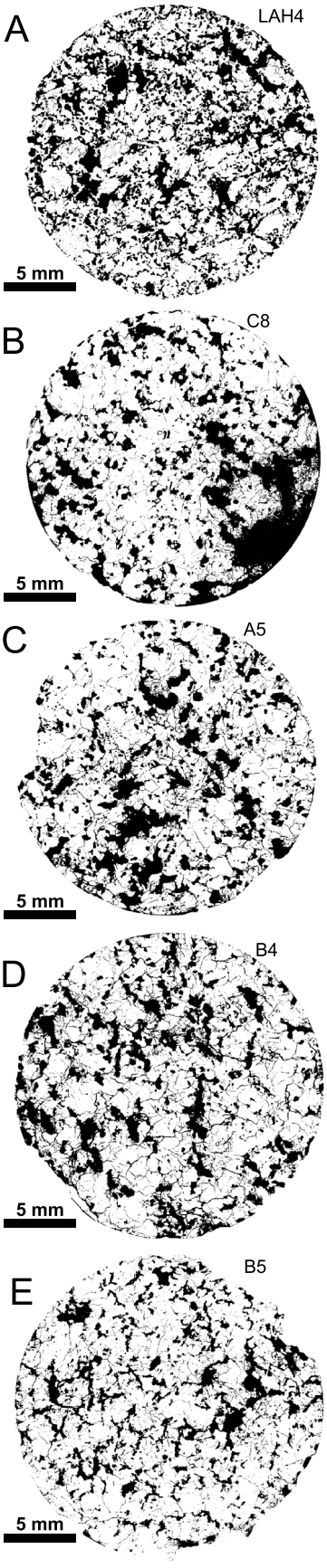

Darcy's law. All measurements were collected under ambient laboratory temperatures.

3.2.6. Uniaxial Compressive Strength Experiments

UCS tests were performed on two cylindrical samples (dried in a vacuum oven at 40°C for at least 24 h prior to experimentation) of similar porosity from each of the five blocks of andesite. The experiments were conducted in a uniaxial press under ambient laboratory conditions at a constant strain rate of $10^{-5}\,s^{-1}$ until failure. During deformation, axial strain, axial stress, and acoustic emissions (AEs) were continuously monitored. Further, the received AE signals were statistically analyzed using the analogous seismic *b* value [*Aki*, 1965] to characterize the nature of the microcracking in our samples.

3.2.7. Thermal Stressing Experiments

Thermal stressing experiments (to 450°C) were performed on cylindrical samples from each of the five blocks of andesite. During thermal stressing, we continuously recorded the furnace temperature, the temperature adjacent to the sample, axial stress, and the output of AE (to be used as a proxy for the initiation and propagation of thermal microcracks). Samples were taken to 450°C at a rate of 1°C/min, held at 450°C for 60 min, and then cooled back to the ambient laboratory temperature at a rate of 1°C/min. Each sample underwent a systematic physical property characterization (see above) before and after thermal stressing (except UCS, which was only determined following thermal stressing). Thin sections of the thermally stressed andesites were also prepared for microcrack density and anisotropy analysis (described in section 3.2.1).

4. Results

4.1. Rock Microstructural Analysis

The photomicrograph maps of each of the andesites (following binary conversion using ImageJ) are presented as Figure 3. As a first-order observation, the andesites are intensely and pervasively microcracked and contain many vesicles.

4.1.1. Microcrack Analyses

Quantitative stereological analysis of the andesites yielded average microcrack densities ranging between 35 and 45 mm^{-1} (Table 2). For an isotropic material (this is confirmed in section 4.2), the microcrack surface area per unit volume S_v can be inferred from the average of the linear intercept measurements in the two directions *P* [*Underwood*, 1970; *Wong*, 1985]:

$$S_v = 2P \quad (1)$$

To visualize the spatial distribution of microcrack surface area density, contour plots of the stereological measurements in the 121 subregions are presented as Figure 4. In most cases, the microcracks appear to be largely homogeneously distributed. Values of S_v reach a maximum of about 90 mm^{-1} in all our samples. Figure 4 shows that, with the

Figure 3. Photomicrograph maps of each of the andesite samples using a transmitted fluorescent light source, converted to binary images using ImageJ. The photomicrographs are all taken in the *XY* plane. The black areas represent the porosity (microcracks and vesicles), and the white areas represent the groundmass/crystals.

Table 2. The Results of the Quantitative Microcrack Density and Anisotropy Analysis on Both As-Collected and Thermally Stressed Samples (450°C) of the Studied Andesites[a]

	B5		B4		A5		C8		LAH4	
Sample	As-Collected	450°C	As-Collected	450°C	As-Collected	450°C	As-Collected	450°C	As-Collected	450°C
P (mm^{-1})	21.1	20.7	21.4	19.2	23.0	22.4	20.4	15.4	12.4	15.5
S_v (mm^{-1})	42.2	41.5	42.7	39.4	46.0	44.7	40.8	30.9	24.8	31.1
Average accuracy of log-log fit (%)	94.86	93.92	94.79	95.25	93.29	94.43	92.83	95.24	94.91	96.61
Anisotropy (with error in %)	1.102 (3.35)	1.055 (2.71)	1.168 (3.99)	1.134 (7.66)	1.002 (2.58)	1.034 (3.13)	1.069 (5.26)	1.046 (4.26)	1.059 (2.93)	1.029 (3.33)
Change in anisotropy (%)	−4.70		−3.40		3.20		−2.30		−3.00	

[a]The first two rows correspond to the optical microscopic method, and the final three rows correspond to the AMOCADO toolbox method. P is the number of linear intercepts per millimeter, and S_v is the microcrack area (in square millimeter) per cubic millimeter. See Appendix A for further details.

exception of LAH4, all of the samples appear to contain approximately the same S_v (see also Table 2).

A detailed examination of the microcrack anisotropy (on the same images) was obtained with the AMOCADO toolbox. The quality of the log-log fits of all 180 fractal regressions for each degree of orientation is between 93% and 97% for each sample (Figure 5 and Table 2). These fits suggest a microcrack network with anisotropy values between 1.002 and 1.168.

4.1.2. Vesicle Analyses

Two-dimensional quantitative vesicle analysis of the andesites yielded average vesicle densities n_A ranging between 3.3 and 8.1 mm^{-2} (Table 3). While vesicle densities are similar for samples A5, B4, and C8 (all between 3.3 and 3.7 mm^{-2}), vesicle densities are much higher in samples B5 (6.1 mm^{-2}) and LAH4 (8.1 mm^{-2}). However, the vesicles of A5, C8, and LAH4 are much larger (average areas ranged between 0.033 and 0.049 mm^2) than those of B4 and B5 (between 0.015 and 0.023 mm^2). The shape of the vesicles in all of the andesites is very similar. Average circularity, aspect ratio, and roundness are about 0.75, 1:1.85, and 0.63, respectively (Table 3). The cumulative relative frequency distributions of the vesicle area and the equivalent vesicle radii for each of the andesites are given as Figure 6, while Figure 7 shows the density n_A of the distribution of vesicle radii for each andesite. We can observe that (1) most vesicle radii lie between 0.01 and 0.1 mm (although the range in size is large) and that (2) B5 contains a larger proportion of smaller vesicles than the other andesites.

4.2. Rock Physical and Mechanical Properties

The rock physical properties (density, porosity, elastic wave velocities, the ratio between P and S wave velocities (the V_P/V_S ratio), elastic moduli, and permeability) of the five andesites are summarized in Table 4.

The connected porosities of the andesites range from about 7 to about 27% (Table 4 and Figure 8). We note that, for these andesites, (1) there is a significant trapped porosity (average of about 2.2% and a maximum of about 4.5%, see Figure 8) and (2) the amount of trapped porosity, in general, increases as total porosity increases (Figure 8b).

Benchtop P and S wave velocities of dry samples range from 2.34 to 3.11 km s^{-1} and 1.09 to 1.45 km s^{-1}, respectively. Using these values, dynamic Young's moduli and Poisson's ratio were calculated to be between 6.4–13.3 GPa and 0.31–0.39, respectively, and V_P/V_S ratios between 1.9 and 2.4. The static Young's moduli (determined from the stress-strain curves), also given in Table 4, range between 8.6 and 31.8 GPa. In general, elastic wave velocities and Young's moduli decrease as porosity increases. The P wave velocity of all the samples greatly increases when the rocks are saturated with distilled water (Table 4). Our elastic wave velocity anisotropy measurements, measured on machined cubes of each material (see section 3.2.3 for details), are presented in Table 5. Our data show that, for each andesite, P and S wave velocities are very similar in the three orthogonal directions, i.e., that the andesites are, within error, seismically isotropic.

Water permeability is plotted as a function of connected water porosity (i.e., the porosity potentially useful for the flow of water) on a log-log scale in Figure 9. The data show that the water permeability of the measured

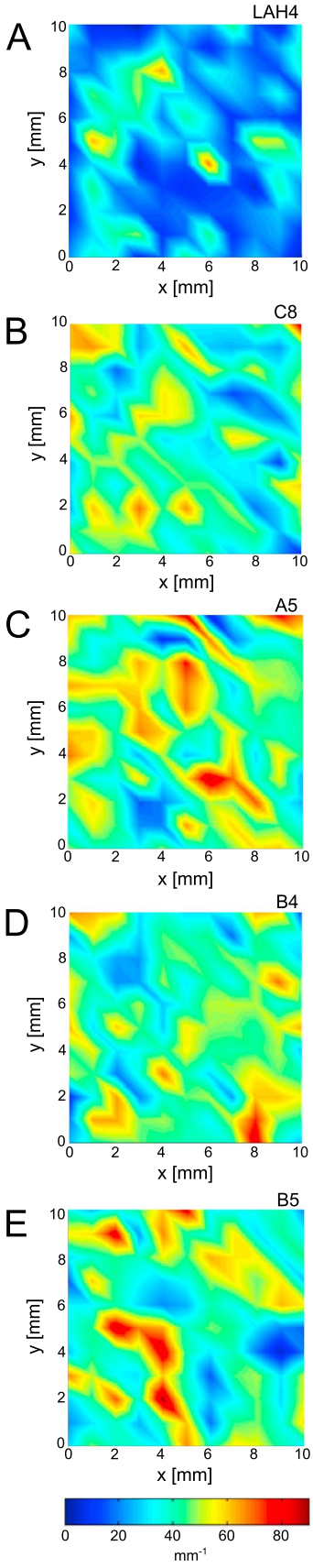

andesites varies between 3.6×10^{-17} and 7.0×10^{-13} m^2. Water permeability increases by about 4 orders of magnitude as porosity is increased by a factor of 3 (from 7 to 24%).

Representative stress-strain curves for each of the studied andesites are presented in Figure 10, together with the AE output during deformation and the evolution of the seismic *b* value. A synoptic plot, showing the stress-strain curves only, is given as Figure 11. The stress-strain curves of Figure 11 show that the andesites exhibit all of the stages of brittle failure in compression. The failure process of brittle rock in compression can be broken down into a number of stages [see *Brace et al.*, 1966; *Hoek and Bieniawski*, 1965; *Scholz*, 1968], characterized by the shape of the stress-strain curve. First, the stress-strain curve is convex; this behavior can be attributed to the closure of microcracks aligned subperpendicular to the direction of loading. Second, the stress-strain curve is very nearly linear as the rock deforms elastically (i.e., recoverable). Third, the stress-strain curve is concave (strain hardening) as the rock is taken to a stress where dilatant microcracks can initiate. Here the rock is deforming inelastically (i.e., nonrecoverably). Fourth, after the peak stress (i.e., the UCS of the material) is reached, there is an axial strain hardening stage before the rock succumbs to failure, usually marked by a substantial stress drop. Post peak behavior ensues, but its observation depends on the stiffness of the testing machine [see *Cook*, 1981]. We note that, although we do not offer complementary tensile strength measurements, the ratio of uniaxial compressive to tensile strength is close to 12 [*Jaeger et al.*, 2007]. In particular, we note that all of the samples show a substantial convex, initial portion. Sample failure is marked by a stress drop (indicating macroscopically brittle behavior) [see *Rutter*, 1986] and is usually accompanied by macroscopic axial splitting (this is especially true for the high-strength, low-porosity samples, see Figure 10). Figure 11 and Table 4 show that the andesites span a large range of UCS (from about 20 MPa for C8 to about 135 MPa for B4).

During deformation, the progression of stress-induced microcracking was monitored via the output of AEs. In our experiments, the rate of AE output increases as the rock approaches failure, and failure is accompanied by a large spike in AE output (Figure 10). The stress at the onset of dilatant microcracking (or C′) [see *Brace et al.*, 1966] was inferred using the AE data (in detail, we selected the point where the AE starts its acceleration to failure). The stress at the onset of C′ ranges between 3.5 and 38 MPa for the andesites of this study (Table 4). However, we suggest that radial strain measurements would help to better constrain C′. As failure approaches, we also observe a decrease in the seismic *b* value, from 1.4–2.0 to 0.4–0.6 at failure. In general, the lower porosity samples exhibit a larger *b* value range. In the experiments where failure was less abrupt, an increase in the *b* value occurs following the peak stress. Photomicrographs of the samples deformed to failure are shown in

Figure 4. The spatial distribution of the specific surface area of the microcracks in the andesite samples. Warm colors (yellow, orange, and red) are indicative of high microcrack surface areas, while cold colors (dark blue and blue) are indicative of low microcrack surface areas.

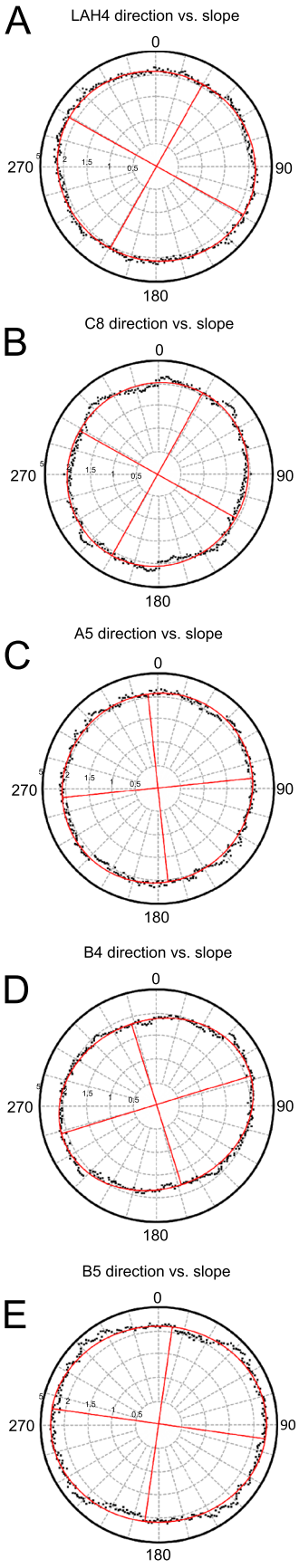

Figure 12. In general, we find that microcracking is significantly increased in all samples (when compared to the as-collected samples of Figure 2). We note (1) that the microcracks are aligned with the direction of the maximum principal stress (i.e., the *Z* direction) and (2) that they often emanate from vesicles (see inset in Figure 12a).

The relationship between rock physical properties (total porosity and *P* wave velocity) and rock mechanical properties (strength) is presented as Figure 13. We note that there is a strong correlation between UCS and total porosity (Figure 13a): UCS increases as total porosity decreases. Although the relationship with *P* wave velocity is less striking, there is still a general trend that UCS decreases as *P* wave velocity decreases (Figure 13b).

4.3. The Influence of Thermal Stressing

The results of the thermal stressing procedure (plots of AE output against time, together with the sample and furnace heating/cooling curves) for each rock type are presented as Figure 14. The results suggest that the AE response of the andesites to thermal stressing varies from sample to sample. Whereas B4 and B5 do not experience much thermal microcracking, LAH4 suffers thermal microcracking during the heating segment only, while C8 and A5 experience thermal microcracking during both the heating and cooling segments. We note that the initiation temperature for thermal microcracking also varies from sample to sample.

Quantitative microstructural analysis has revealed that there is no systematic change in two-dimensional microcrack surface area per unit volume and microcrack network anisotropy upon exposure to 450°C (Table 2). In fact, for the majority of the andesites, the S_v and the microcrack network anisotropy are marginally lower for the thermally stressed samples. We find that thermal stressing only slightly modifies the physical properties of the samples (Table 4). The connected porosities show a modest increase ($< 1\%$), while the V_p/V_s ratios, dry elastic wave velocities, dynamic Young's moduli, and dynamic Poisson's ratios all show a modest decrease (Table 4). We detect no variations (outside the natural variability of the materials) between the strength of the as-collected samples and those thermally stressed (Figure 15 and Table 4). Further, and due to the natural variability between samples, we cannot draw any firm conclusions as to whether thermal stressing has any impact on the onset of dilatancy or static Young's modulus (Table 4).

5. Discussion

5.1. Microstructure of Andesites From Volcán de Colima

Our study has shown that the andesites, representative of those that comprise the volcanic edifice at Volcán de Colima, are pervasively microcracked, as evidenced through microstructural observations and quantitative stereological techniques. Microcrack surface area per unit volume reach values as high as 90 mm^{-1}. To emphasize, the

Figure 5. Crack anisotropy analysis for the andesite samples using the modified Cantor-dust method included in the automated pattern quantification toolbox AMOCADO. Plots are the log-log fits. See Appendix A for details.

Table 3. The Results of the Quantitative Connected Vesicle Size, Shape, and Density Analysis on Each of the Studied Andesites Using ImageJ[a]

	B5	B4	A5	C8	LAH4
Total vesicle area (mm^2)	28.83	26.59	41.46	50.34	84.86
Vesicle porosity (%)	9.2	8.5	13.2	16.0	27.0
Vesicle density (mm^{-2})	6.13	3.69	3.26	3.27	8.13
Average area of a vesicle (mm^2)	0.0150	0.0229	0.0405	0.0490	0.0332
Maximum area of a vesicle (mm^2)	1.108	0.775	2.880	2.535	4.858
Minimum area of a vesicle (mm^2)	0.00019	0.00019	0.00020	0.00021	0.00019
Average equivalent radius (mm)	0.0690	0.0855	0.1136	0.1248	0.1028
Maximum equivalent radius (mm)	0.5938	0.4966	0.9574	0.8982	1.2434
Minimum equivalent radius (mm)	0.00777	0.00770	0.00798	0.00807	0.00780
Average circularity	0.79	0.75	0.76	0.74	0.76
Average aspect ratio	1:1.81	1:1.94	1:1.84	1:1.89	1:1.80
Average roundness	0.65	0.60	0.62	0.62	0.64

[a]See Appendix A for further details.

maximum S_v (using the same method) obtained for a sample of Darley Dale sandstone (porosity = 13%) containing a shear fault was only 40 mm^{-1} [*Wu et al.*, 2000]. Further evidence for high microcrack densities is provided by the pronounced convex shape of the initial portion of the stress-strain curves, generally explained as the closure of subperpendicular microcracks [e.g., *David et al.*, 2011]. Microcrack densities are slightly lower in sample LAH4 (Figure 4), although this could be a product of its high vesicle size and density (Table 3). Microcrack network anisotropy values (that ranged between 1.002 and 1.168), and our *P* wave anisotropy analysis, suggest that the microcrack network is isotropic (for example, anisotropies of 1.353 have been reported for deformed andesitic lavas) [*Lavallée et al.*, 2008]. The isotropic nature of the microcrack network suggests that the microcracking may be of thermal origin. Thermal microcrack networks are often isotropic (for initially isotropic materials), while mechanical microcracking normally produces an anisotropic crack network [see *David et al.*, 1999]. We therefore propose that the pervasive microcrack network is the result of the relatively rapid cooling history associated with their eruptive origin. A similar conclusion was drawn in reference to a highly microcracked basaltic lava from Mount Etna [*Vinciguerra et al.*, 2005]. Despite the large natural variability in connected water porosity (7 to 27%), the microcrack surface area densities of the andesites are remarkably similar (with the exception of LAH4). This implies (1) that the cooling histories of these andesites were similar and (2) that the differences in porosities must largely be due to a variable vesicle density and/or vesicle size. Indeed, we note that the two-dimensional vesicle porosity or vesicularity (Table 3) is very close to the average connected water porosities listed in Table 4. This is largely to be expected, since the extremely low aspect ratio of microcracks makes them inefficient at generating porosity (although their effect on physical and mechanical properties can be significant, see section 5.2).

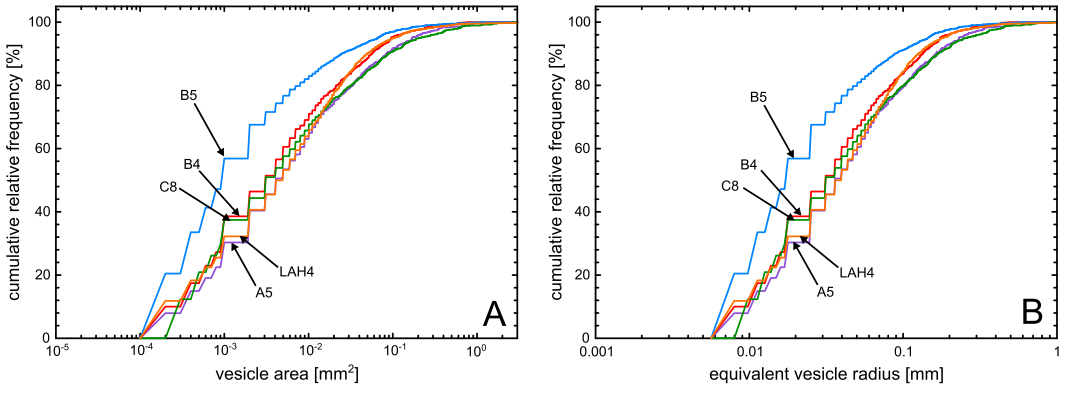

Figure 6. Cumulative relative frequencies of (a) vesicle area and (b) equivalent vesicle radius for each of the andesites. Blue–B5; red–B4; green–C8; orange–LAH4; purple–A5.

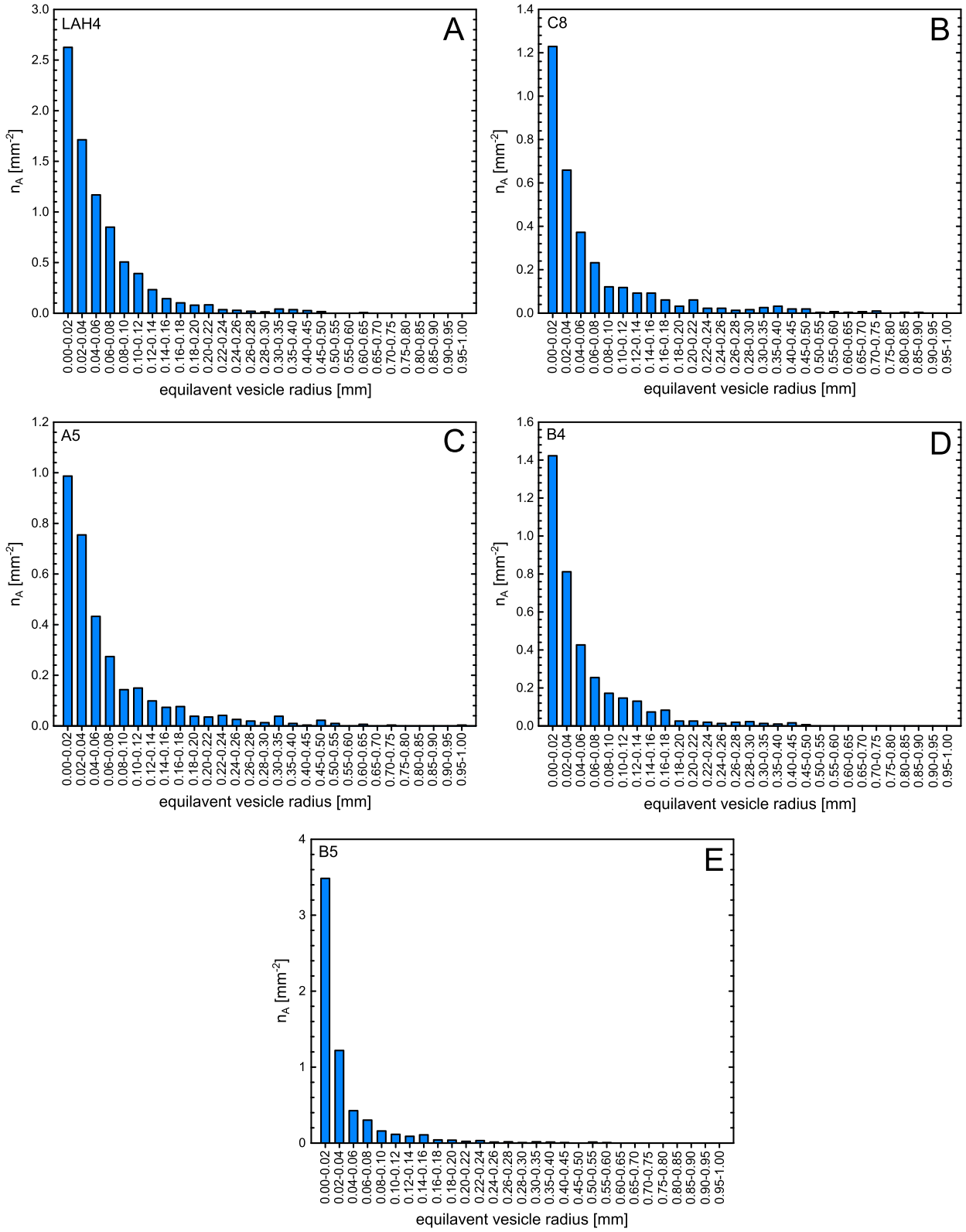

Figure 7. Equivalent vesicle radius densities for each of the andesites. The histogram bars represent 0.02 mm intervals up to 0.30 mm; after 0.30 mm the interval increases to 0.05 mm. Note that, to show the full vesicle radius distribution for each andesite, the *y* axes are not always identical.

Journal of Geophysical Research: Solid Earth

10.1002/2013JB010521

Table 4. Average Physical and Mechanical Properties of the Andesites Investigated in This Study: Bulk Sample Density, Connected Water Porosity, Elastic Wave Velocities, Water Permeability, Dynamic Young's Modulus and Poisson's Ratio, Static Young's Modulus, Uniaxial Compressive Strength (UCS), and the Stress at Which C′ Was Observed in Our Acoustic Emission Data (C′ Is Not an Average, It Is Just the Data From Figure 10)[a]

		B5		B4		A5		C8		LAH4	
Sample		As-Collected	450°C	As-Collected	450°C	As-Collected	450°C	As-Collected	450°C	As-Collected	450°C
Bulk sample density (g/cm^3)	Dry	2.48		2.48		2.40		2.13		1.96	
	Water-saturated	2.53		2.50		2.48		2.30		2.21	
Connected water porosity (%)		7.9	8.1	8.6	8.9	11.2	11.6	17.6	17.7	25.0	25.2
Total porosity (%)		12.1	-	14.0	-	14.3	-	23.8	-	29.8	-
P wave velocity (km s^{-1})	Dry	3.11	2.71	2.69	2.52	3.11	2.85	2.56	2.31	2.34	1.89
	Water-saturated	4.84	4.67	4.98	4.96	4.97	4.78	4.30	4.31	3.91	4.01
S wave velocity (km s^{-1})	Dry	1.30	1.23	1.42	1.33	1.45	1.34	1.24	1.21	1.09	1.00
V_P/V_S ratio	Dry	2.39	2.19	1.90	1.77	2.21	2.15	2.07	1.90	2.15	1.89
Dynamic Young's modulus (GPa)	Dry	11.8	10.4	13.0	11.3	13.3	11.5	8.8	8.2	6.4	5.1
Dynamic Poisson's ratio	Dry	0.39	0.36	0.31	0.26	0.33	0.34	0.35	0.30	0.36	0.30
Static Young's modulus (GPa)	Dry	21.6[b]	23.1[b]	31.8[b]	35.6[b]	23.6[b]	23.8[b]	8.6[b]	9.9[b]	9.2[b]	11.6[b]
Water permeability (m^2) at Pc = 2 MPa	Water-saturated	1.62×10^{-16}	-	8.64×10^{-17}	-	2.55×10^{-16}	-	1.08×10^{-12}	-	1.45×10^{-12}	-
Uniaxial compressive strength (MPa)	Dry	87.5	86.3	124.0	128.8	74.0	88.1	23.9	30.5	29.9	35.4
C′ (MPa)	Dry	38.0	28.5	19.2	19.6	9.8	14.0	3.5	5.8	7.5	12.4

[a]Data for both as-collected and thermally stressed (450°C) samples are shown. "Dry" and "water-saturated" refer to measurements on samples dried in a vacuum oven at 40°C and samples saturated with distilled water in a vacuum, respectively. Elastic wave velocities (and therefore the resultant dynamic elastic moduli), UCS, permeability, and static Young's modulus have been determined in the *Z* direction. The physical property characterization was performed under the lowest possible stress conditions (to avoid damaging the samples). The bulk densities and porosities were measured at ambient pressure, the elastic wave velocities and dynamic moduli were determined using an axial stress of 1.9 MPa, and permeability was measured at a confining pressure of 2 MPa.

[b]The static Young's moduli was measured at axial stresses between 15 and 100 MPa, depending on the strength of the sample. Therefore, direct comparison with the dynamic Young's moduli is ill-advised (see text for details).

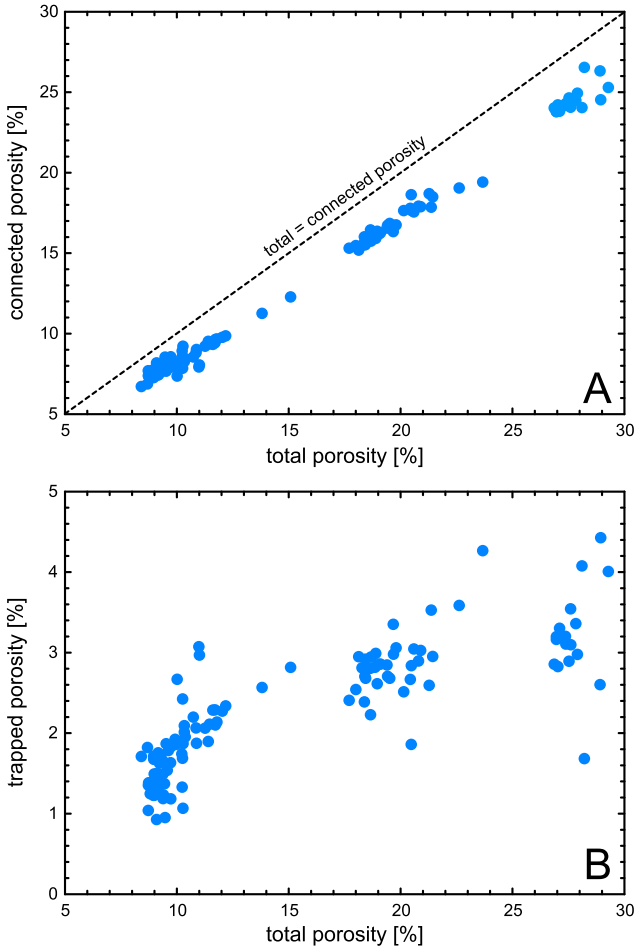

Figure 8. (a) The connected porosity as a function of the total porosity for the studied andesites (dashed line is the 1:1 line). (b) The trapped porosity as a function of the total porosity for the studied andesites.

Although our study has highlighted that andesites from Volcán de Colima contain high vesicle densities, a distinguishing feature of these materials, when compared with nonvolcanic rocks, is the extremely large range of vesicle or pore sizes (radii between 0.008 and 1.24 mm). For nonvolcanic rocks, this range of pore size is largely unprecedented. Similar analyses on limestones (that analyze pores with radii larger than 0.003 mm) showed that the pores have radii between 0.003 and 0.015 mm [*Vajdova et al.*, 2010] and 0.003 and 0.25 mm [*Vajdova et al.*, 2012]. However, while limestones typically contain a significant micropore contribution (i.e., below the resolution of the analyses), we note that our two-dimensional porosities (Table 3) were very similar to those calculated using the triple-weight water saturation technique (Table 4), suggesting that, in the measurements presented in this study, we captured most, if not all, of the vesicularity. For volcanic rocks, the range of vesicle size can range from the submicron scale to the meter scale [e.g., *Walker*, 1989; *Shea et al.*, 2010, and references therein]. While a detailed textural description of the vesicles is beyond the scope of this study (our blocks were collected from a block-and-ash flow, lahar flow, and lava deposits), one interesting aspect of the vesicles is that they are not circular (average vesicle circularity for the andesites was between 0.74 and 0.79, Table 3). Departure from noncircularity could be the result of deformation within the conduit, although we note that there is no preferred vesicle shape orientation (Figure 2).

5.2. Physical and Mechanical Properties of Andesites From Volcán de Colima

The complex microstructure (pervasive microcrack network, large vesicle size, and high vesicle density) of these andesites severely impacts their rock physical and mechanical properties.

5.2.1. Density and Porosity

Bulk sample densities are low and porosities are high as a result of the combined presence of microcracks and vesicles. The complexity of these andesites is emphasized by their substantial trapped porosities, although this is not unexpected for volcanic rocks [e.g., *Bernard et al.*, 2007]. We note that while such trapped porosity could play an important role for some physical and mechanical properties (elastic velocities, strength, and elastic moduli) others, such as water permeability, rely only on the connected water porosity.

5.2.2. Elastic Wave Velocities

The andesites have very low elastic wave velocities (*P* and *S* wave velocities range from 2.34 to 3.11 km s^{-1} and 1.09 to 1.45 km s^{-1}, respectively). For comparison, the *P* and *S* wave velocities of an aphyric basalt from Seljadur (Iceland; porosity = 4.5%) are 5.43 and 3.03 km s^{-1}, respectively [*Vinciguerra et al.*, 2005]. The elastic wave velocities are low for these andesites because they are very sensitive to microcrack porosity [e.g., see *O'Connell and Budiansky*, 1974], much more so than vesicle porosity. For instance, the *P* wave velocity of the aforementioned basalt from Iceland can be reduced by almost 60% by thermal microcracks alone

Table 5. Elastic Wave Velocities in the *X*, *Y*, and *Z* Directions for All of the Studied Andesites

	B5		B4		A5		C8		LAH4	
	P Wave Velocity (km s^{-1})	*S* Wave Velocity (km s^{-1})	*P* Wave Velocity (km s^{-1})	*S* Wave Velocity (km s^{-1})	*P* Wave Velocity (km s^{-1})	*S* Wave Velocity (km s^{-1})	*P* Wave Velocity (km s^{-1})	*S* Wave Velocity (km s^{-1})	*P* Wave Velocity (km s^{-1})	*S* Wave Velocity (km s^{-1})
X	2.69	1.23	2.62	1.40	2.43	1.31	2.39	1.23	2.41	1.15
Y	2.81	1.25	2.70	1.42	2.34	1.40	2.45	1.22	2.43	1.20
Z	2.73	1.26	2.59	1.35	2.38	1.47	2.46	1.19	2.46	1.19
V_{max}/V_{min}	1.04	1.02	1.04	1.05	1.04	1.12	1.03	1.03	1.02	1.04

[*Vinciguerra et al.*, 2005]. We also find that the *P* wave velocity of the andesites increased significantly upon water saturation (*P* waves travel faster through water than air). This corroborates with the fact that the microcracks are a significant contributor to the low elastic wave velocities, as, upon their saturation, *P* wave velocity would be expected to increase significantly (for the andesites of this study, *P* wave velocities were increased from the above-quoted values to between 3.91 and 4.97 km s^{-1}, see Table 4).

5.2.3. Young's Modulus

The stiffness (Young's modulus) of these andesites is very low (dynamic and static Young's moduli ranged between 6.38 and 13.34 GPa and 9.05 and 34.17 GPa, respectively). For comparison, the static Young's modulus of an aphyric basalt from Iceland was measured to be 66.5 GPa [*Heap et al.*, 2010]. It has long been established that static and dynamic elastic moduli differ, due to the large difference in frequency [e.g., *Simmons and Brace*, 1965; *Cheng and Johnston*, 1981; *Eissa and Kazi*, 1989; *Ciccotti et al.*, 2000; *Ciccotti and Mulargia*, 2004]. However, dynamic moduli are commonly much higher than static moduli, particularly when the rock is highly fractured [e.g., *Gudmundsson*, 2011]. The opposite appears to be true for the andesites of this study (under the implemented experimental conditions, see Table 4). We note, however, that the moduli were calculated at different axial stresses. The dynamic moduli were calculated from elastic wave velocities measured at 1.9 MPa whereas the static moduli were calculated using stress-strain data between 15 and 100 MPa, depending on the stress level at which the slope of the stress-strain curve is at a maximum. This may preclude direct comparison. In an attempt to resolve this issue, we performed a pilot experiment in which we measured the static (tangent) and dynamic Young's modulus at the same axial stress (Figure 16). We note that both moduli increase with increasing axial stress (although the static values below about 25 MPa are, as per our definition, not strictly static elastic moduli). Figure 16 aptly shows that (1) when the moduli are compared at the same level of stress, the dynamic modulus is always significantly higher than the static modulus (as reported by previous studies on a variety of rock types) [see *Gudmundsson*, 2011] and (2) the dynamic modulus measured at 1.9 MPa (the stress used for the physical property characterization, see Table 4) is lower than the static modulus measured using the method outlined in Appendix A (in this case, 30 MPa). These observations can be explained by the progressive closure of microcracks during stressing. These results clearly demonstrate that for pervasively microcracked materials such as the andesites of this study, static and dynamic Young's moduli should only be compared when measured at the same stress.

5.2.4. Permeability

The water permeability of these andesites is high (up to ~10^{-13} m^2) and increases as connected water porosity increases (Figure 9). Water permeability measurements on andesites from Volcán de Colima have been previously measured to be within the range of ~10^{-13} to ~10^{-16} m^2 [*Kolzenburg et al.*, 2012; *Kendrick et al.*, 2013]. As a comparison, low-porosity (4.5%) aphyric basalts can have a water permeability as low as ~10^{-21} to ~10^{-19} m^2 [*Vinciguerra et al.*, 2005; *Nara et al.*, 2011]. The permeability of volcanic rocks has been shown to display an extremely wide range, owing to the vast assortment of microstructures. For example, the gas permeability of porous (35–94%) pumices have been measured to be in the range of ~10^{-13} to ~10^{-10} m^2 [*Klug and Cashman*,

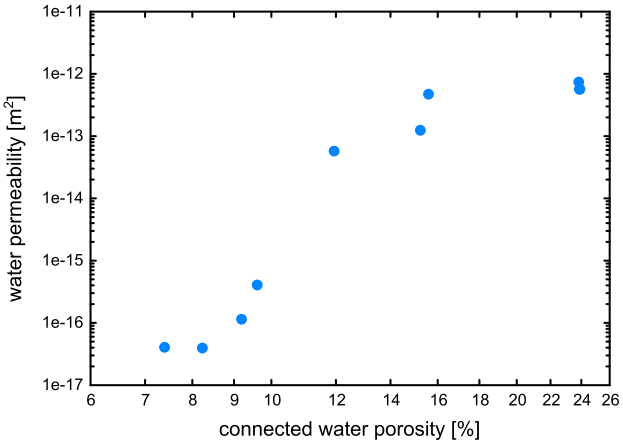

Figure 9. The water (distilled water) permeability of andesites from Volcán de Colima as a function of connected water porosity, plotted on log-log axes.

1996; *Rust and Cashman*, 2004; *Mueller et al.*, 2005; *Wright et al.*, 2006; *Bernard et al.*, 2007; *Wright and Cashman*, 2013]. However, the gas permeability of effusive volcanic rocks demonstrate a much wider range: ~10^{-17} to ~10^{-11} m^2 [*Saar and Manga*, 1999; *Rust and Cashman*, 2004; *Mueller et al.*, 2005; *Bernard et al.*, 2007]. A compilation of data on both explosive and effusive rocks is presented in *Wright et al.* [2009]. Several of these studies have described their data using a single power law; however, a close examination of our data reveals that there are two families with different permeability-porosity power law exponents (Figure 19a). The low-porosity (7–12%) family has an exponent of about 15.9 and the high-porosity (15–24%) family has an exponent of about 3.2. The crossover porosity, where the two trends meet, is in the range of 11–14%. The permeability-porosity relationship of the andesites is similar to that of Fontainebleau sandstone [*Bourbié and Zinszner*, 1985]. The power law exponent of Fontainebleau sandstone was increased from 3.05 to 7.33 below a crossover porosity of about 9%. The existence of a crossover porosity for rocks from Volcán de Colima is emphasized when one compiles the available published data (Figure 19c). For volcanic rocks, it is clear that a simple relationship between porosity and permeability simply does not exist. To emphasize, two volcanic rocks (porosities as different as 3 and 85%) can both have permeabilities on the order of ~10^{-12} m^2 (see compilation in *Mueller et al.* [2008]). The permeability of andesites from Volcán de Colima is discussed further in sections 5.3.2 and 5.5.

5.2.5. Uniaxial Compressive Strength

The UCS of the studied andesites, in comparison to other rocks, is low. It must be noted that while typical values of UCS for low-porosity (< 1%) granitic rocks are about 205–240 MPa [e.g., *Heap and Faulkner*, 2008; *Blake et al.*, 2013], the UCS of volcanic rocks can be extremely variable (see the examples in Table 6), a result of their varied composition and microstructure. We note that the strengths of the andesites of this study, in comparison to those volcanic rocks in Table 6, are still low (with the exception of the highly porous tuffs). This is a result of their highly microcracked and porous nature. We also note that we observe a decrease in *b* value as sample failure is approached (Figure 10). A decrease in *b* value indicates that the proportion of large cracking events increased as failure was approached (as observed previously for other volcanic rocks) [see *Smith et al.*, 2009]. The reincrease following sample failure is likely to represent smaller-scale microcracking occurring on the newly formed macroscopic fractures.

The relationship between physical and mechanical properties of the andesites is illustrated in Figure 13. It is well known in experimental rock deformation that the strength of rock decreases as porosity increases [*Zoback*, 2010; *Baud et al.*, 2014]. A conclusion also resolved in experimental volcanology [*Spieler et al.*, 2004], although the relative contributions from microcrack porosity and vesicularity remains unconstrained. This premise entails that rock strength should decrease with increasing preexisting "damage" (a combination of microcracks and pores/vesicles). The relationship between *P* wave velocity and UCS is more clouded (Figure 13b); although there is a general trend where UCS decreases as *P* wave velocity decreases. Similar cloudy *P* wave velocity-UCS relationships have also been observed for sedimentary rocks [*Chang et al.*, 2006]. Microcrack density and *P* wave velocity are intrinsically connected (for instance, it is possible to invert ultrasonic velocities to calculate microcrack densities) [see *Schubnel et al.*, 2006]. Therefore, if one were to increase microcrack porosity in a material without vesicles, the relationship between UCS and *P* wave velocity should be more clear-cut. In the case of andesites from Volcán de Colima (Figure 13b), it is therefore clear that microcracks alone are not controlling the reduction in strength. This is corroborated by the fact that (1) microcrack densities do not differ greatly between the andesites (Table 2) and (2) failure in compression may be heavily influenced by vesicle-emanating microcracking (Figure 12a, see also the next section).

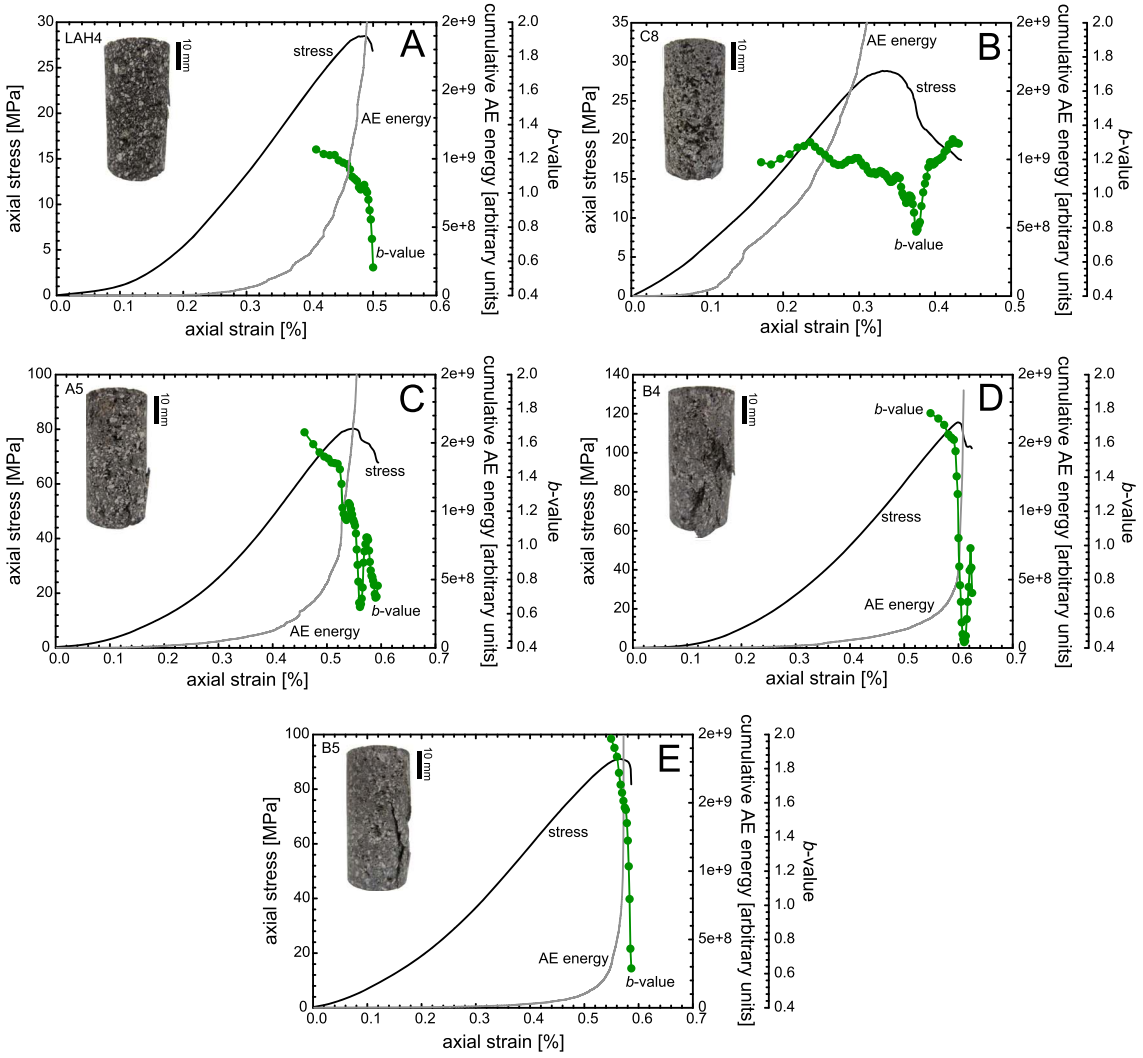

Figure 10. Stress-strain curves for the andesite samples from constant strain rate (1.0×10^{-5} s^{-1}) uniaxial deformation experiments. Data are plotted with the cumulative acoustic emission "energy" and the evolution of the seismic *b* value. Photographs of the post failure samples are also included on the graphs. Note that the axial stress and axial strain axes are not always identical.

5.3. Application of Micromechanical and Geometrical Permeability Models

While extracting empirical relationships between rock properties may appear inviting (e.g., the relationships presented in Figures 9 and 13), we advise extreme caution based on their lack of physical basis (the parameters are not easily related to independently measurable quantities). For volcanic rocks this is especially true, since their genesis and therefore microstructure can vary significantly. Micromechanical and geometrical permeability models hold the potential to be better constrained as their parameters often have a clear physical meaning. In this section, we perform a pilot study to test the applicability of micromechanical modeling (pore- and wing-crack modeling) [see *Sammis and Ashby*, 1986; *Ashby and Sammis*, 1990] and geometrical permeability modeling (using the Kozeny-Carman equation) [see *Kozeny*, 1927; *Carman*, 1937; *Guéguen and Palciauskas*, 1994]. In fact, the andesites of this study represent the ideal case to test such models since (1) their chemical composition is identical (Table 1) and (2) they are all products of the same volcano.

5.3.1. Micromechanical Modeling: Pore- and Wing-Crack Modeling

Micromechanical modeling can provide useful insights in the mechanics of compressive failure in brittle rock [*Wong and Baud*, 2012]. However, they have rarely been applied to volcanic rocks [e.g., *Zhu et al.*, 2011; *Vasseur et al.*, 2013]. In most cases, the microstructure can be idealized in terms of an inclusion model with

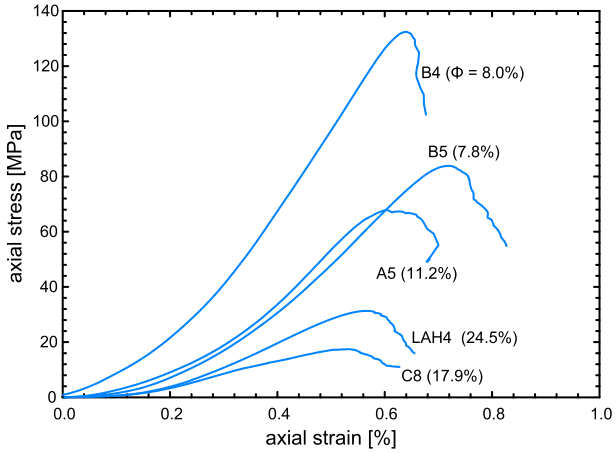

Figure 11. Synopsis plot showing representative stress-strain curves for all the andesite blocks. The porosity of each sample is provided next to the relevant curve.

microcracks or equant vesicles embedded in an elastic continuum. The preexisting microcracks or vesicles act as stress concentrators for the initiation of extensile cracks which then propagate through the porous medium. The mechanical behavior is controlled by the evolution of such damage. The initiation and propagation of these stress-induced microcracks can be analyzed using linear elastic fracture mechanics [*Wong and Baud*, 2012]. Since the andesite samples contain both microcracks and vesicles (see Figures 2b and 2c), we performed a pilot study to test the applicability of two micromechanical models: one that considers only vesicles (the pore-emanated crack model of *Sammis and Ashby* [1986]) and one that considers only microcracks (the sliding wing-crack model of *Ashby and Sammis* [1990]). If the experimental data can be adequately described by one of these models, and not the other, then we can glean information regarding

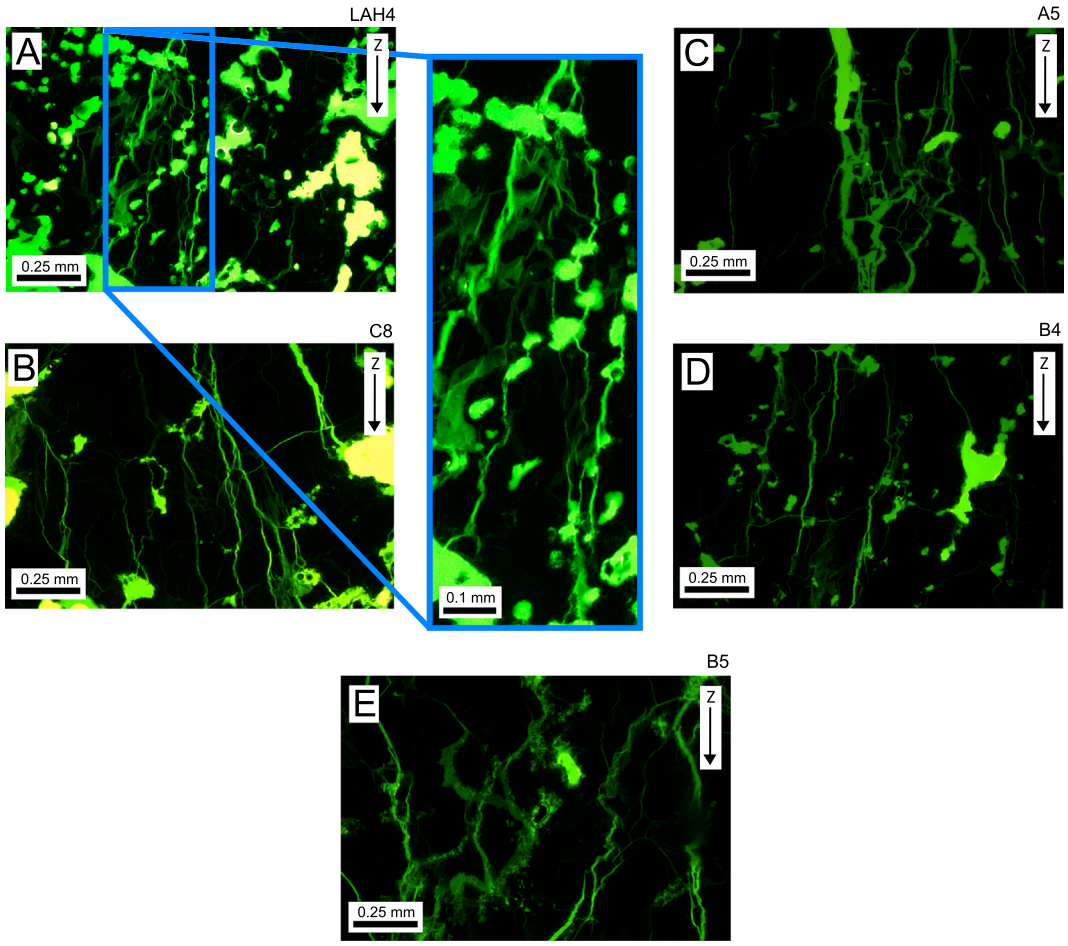

Figure 12. (a–e) Photomicrographs of the andesite samples deformed to failure during uniaxial compression tests, using a transmitted fluorescent light source. The inset in Figure 12a zooms in on vesicle-emanated microcracking. The light green areas represent the porosity (microcracks and vesicles), and the dark green/black areas represent the solid rock (groundmass/crystals).

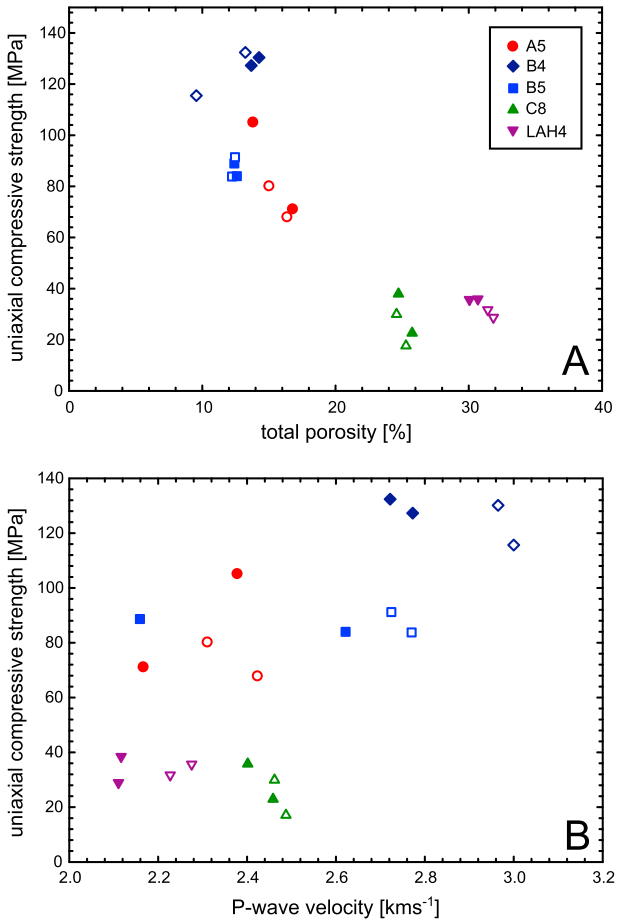

Figure 13. The relationship between uniaxial compressive strength and (a) total porosity and (b) *P* wave velocity.

the control of the microcracks and the vesicles on the strength of these materials in compression. Unfortunately, a model that combines both elements is yet to be formulated.

The pore-emanated crack model of *Sammis and Ashby* [1986] describes a two-dimensional elastic medium populated by circular holes of uniform radius *r*. As the applied stress (σ) increases, cracks emanate from the circular holes (parallel to the direction of the applied stress) when the stress at the tip of a small crack on the circular surface reaches a critical value (K_{IC}, the critical stress intensity factor or "fracture toughness"). The newly formed cracks propagate to a distance *l* in the direction of the maximum principal stress. Once the cracks are long enough, they can interact, thus increasing the local tensile stress intensity. Eventually, they coalesce and conspire to induce the macroscopic failure of the elastic medium (Figures 17a–17c). In the case of uniaxial compression, *Zhu et al.* [2010] derived an analytical approximation of *Sammis and Ashby*'s [1986] pore-emanated crack model to estimate UCS (σ_p, the peak stress) as a function of the bulk sample porosity (φ):

$$\sigma_p = \frac{1.325}{\varphi^{0.414}} \frac{K_{IC}}{\sqrt{\pi r}} \quad (2)$$

Alternatively, the sliding wing-crack model (Figures 17d–17f) considers the tensile stress concentrators to be the tips of inclined (45°) preexisting cracks (of length 2*c*) undergoing frictional slip [*Horii and Nemat-Nasser*, 1986; *Ashby and Sammis*, 1990; *Kemeny and Cook*, 1991]. Similar to the pore-emanating crack model, the inclined cracks populate a two-dimensional elastic medium. However, the frictional resistance of the closed crack must first be overcome, by shear traction induced by an applied stress, before the wing cracks can propagate (parallel to the direction of the applied stress). As before, the wing cracks cannot propagate until K_{IC} is exceeded. In the case of uniaxial compression, another analytical estimate was also inferred for σ_p [*Baud et al.*, 2014]:

$$\sigma_p = \frac{1.346}{\sqrt{1+\mu^2}-\mu} \frac{K_{IC}}{\sqrt{\pi c}} D_0^{-0.256} \quad (3)$$

where μ is the friction coefficient of the sliding crack and D_0 is an initial damage (a function of the angle of the initial microcrack with respect to the maximum principal stress and the initial number of sliding cracks per unit area) [*Ashby and Sammis*, 1990]. It should also be noted that in both models, a comparable term (the ratio of the fracture toughness over the square root of the default size) appears.

The predictions of the pore-emanated crack model are presented on a plot of total porosity against UCS in Figure 18. Our experimental data could not be fitted using a single value of $\frac{K_{IC}}{\sqrt{\pi r}}$ but can be bracketed between two theoretical curves where $\frac{K_{IC}}{\sqrt{\pi r}}$ equals 7 and 44 MPa. In detail, the data can be divided into two groups (excluding the much stronger B4 samples): (1) high-porosity end-members (LAH4 and C8) that can be bracketed between theoretical curves where $\frac{K_{IC}}{\sqrt{\pi r}}$ equals about 7 and 17 MPa and (2) low-porosity end-

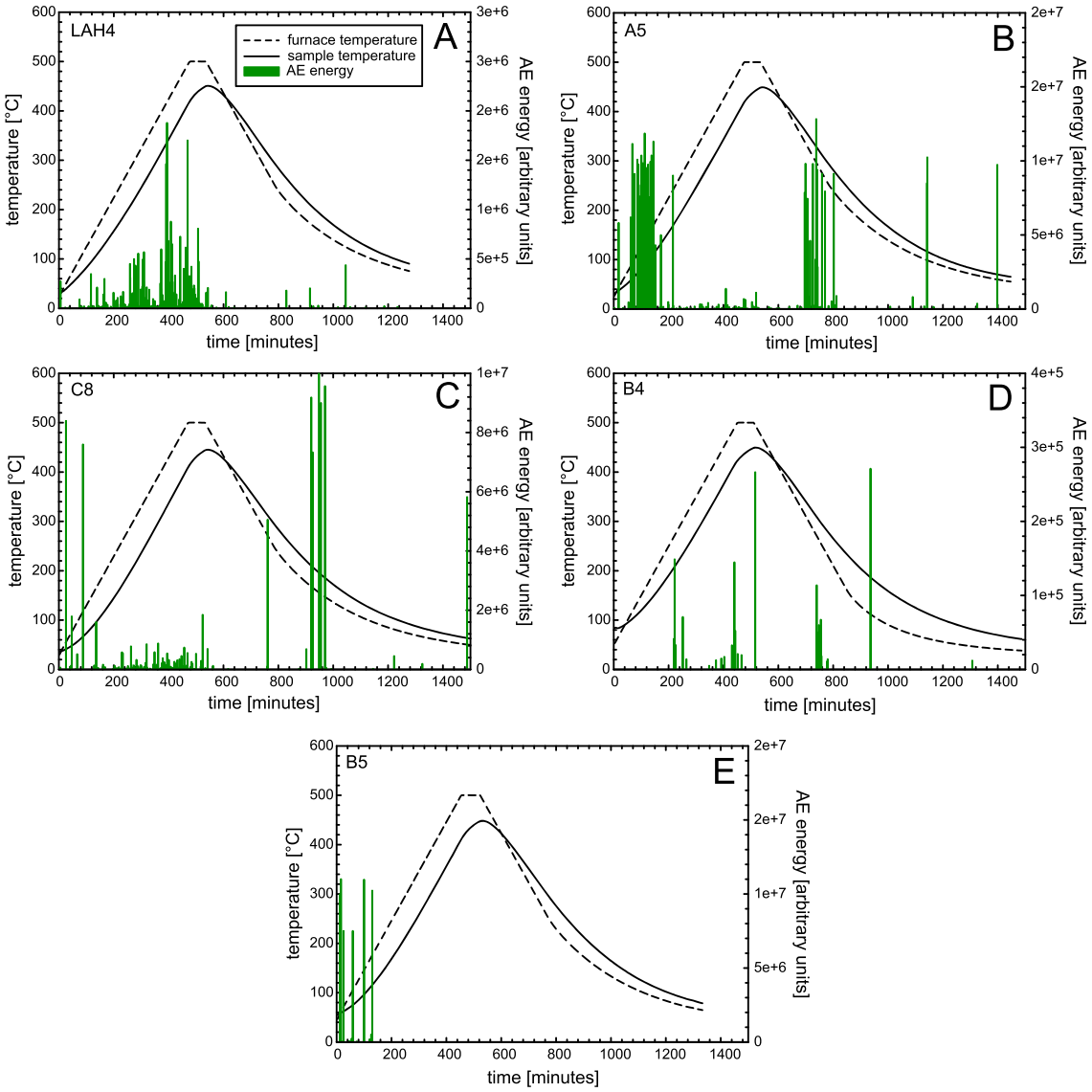

Figure 14. Acoustic emission energy (the area under the received AE waveform envelope) in 1 min bins, sample temperature, and furnace temperature against time for each of the studied andesites during our thermal stressing experiments. Note that the acoustic emission energy axes are not the same between samples.

members (A5 and B5, excluding the A5 sample with a UCS of 105.1 MPa) that can be bracketed between curves where $\frac{K_{IC}}{\sqrt{\pi r}}$ equals about 24 and 29 MPa. If we assume a fixed value r (using the average equivalent vesicle radius for each andesite, Table 3) we can estimate the range of K_{IC} for these rocks, and likewise, if we assume a fixed value for K_{IC} we can investigate the range of r. The inferred values of K_{IC} range from 0.40 to 2.28 MPa $m^{-1/2}$; we obtained low values for the high-porosity andesites (K_{IC} = 0.40–1.06 MPa $m^{-1/2}$) and high values for the low-porosity andesites (K_{IC} = 1.12–2.28 MPa $m^{-1/2}$). Previous studies on andesite reported a value of K_{IC} of about 1.5–2.0 MPa $m^{-1/2}$ [*Ouchterlony*, 1990; *Obara et al.*, 1992; *Keles and Tutluoglu*, 2011; *Nara et al.*, 2012]. The values inferred for the low-porosity andesites are therefore in qualitative agreement with these data. However, the inferred values of K_{IC} for the high-porosity andesites are significantly lower than those previously reported in the literature. This suggests that, beyond a certain porosity, the larger vesicles may play a more dominant role in the failure process than the average vesicle size. To conclude, although the pore-crack model seems to capture part of the phenomenology of brittle failure in the andesites (excluding the B4 samples), new laboratory experiments should now be performed to constrain K_{IC} and check the quantitative prediction of this model.

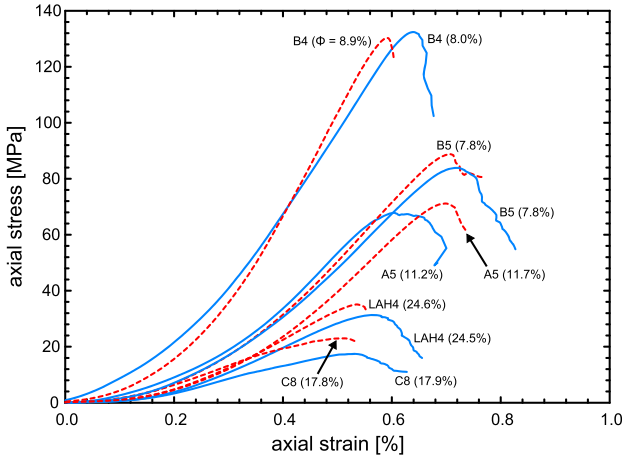

Figure 15. Synopsis plot showing representative stress-strain curves for all the as-collected andesites (the same as those in Figure 11, solid blue lines), together with representative stress-strain curves for the thermally stressed andesite samples (red dashed lines). The porosity of each sample is provided next to the relevant curve.

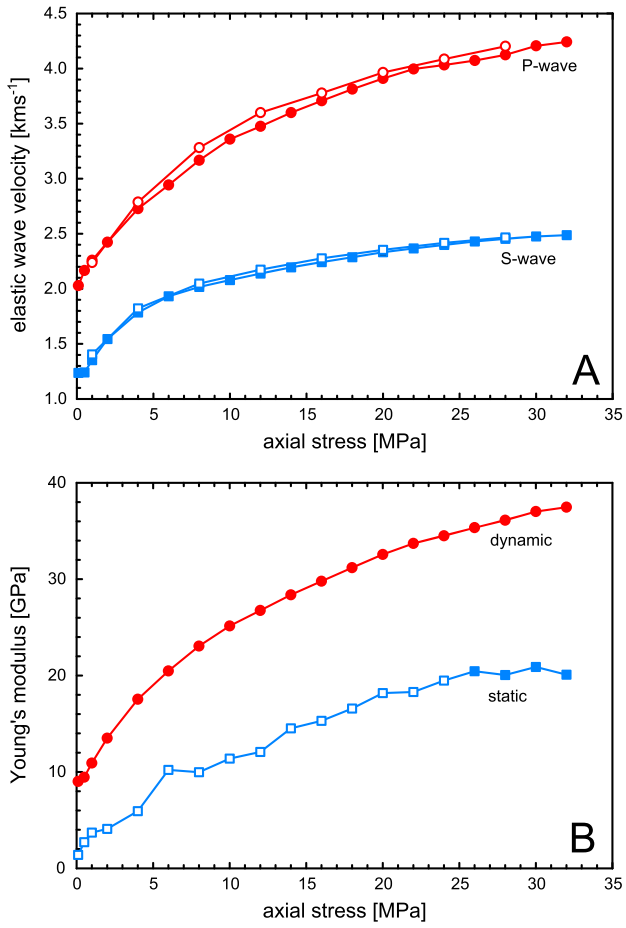

Figure 16. The evolution of (a) *P* and *S* wave velocities and (b) dynamic and static Young's moduli with increasing axial stress. The experiment was performed on a sample of A5 (porosity = 9.2%) using the uniaxial compression apparatus (Figure A2). Modified endcaps containing piezoelectric crystals were used to measure *P* and *S* wave velocities. The unfilled shapes in Figure 16a are measurements taken during the unloading of the sample, showing that the process is reversible. The unfilled shapes in Figure 16b highlight the static moduli that, according to our definition, are not strictly elastic moduli; we include them here for completeness.

Table 6. Values of Porosity and Uniaxial Compressive Strength for Various Volcanic Rocks

Rock Type	Connected Porosity (%)	Uniaxial Compressive Strength (MPa)	Reference
Etna basalt	4.4	140	*Heap et al.* [2009]
Icelandic basalt	4.5[a]	360	*Heap et al.* [2010]
Vesuvian basalt	8–10	86–93	*Rocchi et al.* [2004]
Etnean basalt	8–10	102–138	*Rocchi et al.* [2004]
Stromboli basalt	13[a]	100	*Heap et al.* [2010]
Mount Shasta andesite	7.2	82–125	*Smith et al.* [2009]
Colima andesite	8–11	115–138[b]	*Kolzenburg et al.* [2012]
Mount Saint Helen's andesite	9.5	140	*Smith et al.* [2011]
Mount Hood andesite	10–12	120	*Bauer et al.* [1981]
Kumamoto andesite	13[a]	130	*Jeong et al.* [2007]
Neapolitan Yellow Tuff	44	3.5	*Heap et al.* [2012]
Piperno Tuff	48	1.6	*Heap et al.* [2012]
Welded Grey Ignimbrite	49	9	*Heap et al.* [2012]

[a]The porosity was remeasured (and therefore is different from the porosity quoted in the original study; the porosity of Kumamoto andesite was not quoted in *Jeong et al.* [2007]).
[b]The measurements were performed at in situ temperatures of 940°C. We include these data here for two reasons: (1) they were measured on the most pertinent rock type and (2) the materials were not glassy and, even at 940°C, behavior was entirely brittle [see *Kolzenburg et al.*, 2012].

Considering that the andesite samples all have a high microcrack density (Table 2), another possibility would be to assume that the microcracks play the dominant role in their brittle failure in compression. To test this theory, we can use the sliding wing-crack model (Figures 17d–17f) [*Horii and Nemat-Nasser*, 1986; *Ashby and Sammis*, 1990]. The predicted UCS (σ_p) given by equation (3) contains four parameters: K_{IC}, m, c, and D_0. We can partially constrain these parameters using the stress at which we inferred the onset of dilatancy, C′ (i.e., the onset of the acceleration in AE activity, see Figure 10). Assuming that C′ corresponds to the propagation of the most favorably orientated microcracks, the stress at the onset of dilatancy ($\sigma_{C'}$) predicted by the wing-crack model [*Ashby and Sammis*, 1990; *Baud et al.*, 2000] is given by

$$\sigma_{C'} = \frac{\sqrt{3}}{\sqrt{1+\mu^2}-\mu}\frac{K_{IC}}{\sqrt{\pi c}} \tag{4}$$

The initial damage D_0 can be inferred directly from

$${D_0}^{0.256} = 0.777\frac{\sigma_{C'}}{\sigma_p} \tag{5}$$

Using the data of Table 4, we find that $D_0 < 0.012$ for all the andesites. However, these values are significantly lower than the results compiled for rocks by *Paterson and Wong* [2005], including some low-porosity (< 1%) end-members such as Westerly granite. Our inferred values for D_0 are therefore suspiciously low for such pervasively microcracked and porous rocks. Several factors could explain this discrepancy. First, our estimation hinges on the precise determination of C′, which is difficult when relying only on AE data (C′ can be more accurately determined using radial strain data). Second, equation (5) assumes that the microcracks involved in the dilatancy process are those involved in the failure process. *Baud et al.* [2014] recently suggested that this assumption may well be invalid for materials with complex mineralogy and microstructure and that consequently the crack lengths and/or the K_{IC} considered in equations (3) and (4) could be different. It is clear that more laboratory data are now needed to better constrain the model parameters and to verify its applicability to these materials.

In summary, the micromechanical analysis of uniaxial data from a suite of andesites from Volcán de Colima suggests that the pore-emanated crack model is more appropriate than the sliding wing-crack model. This is consistent with the fact that our microstructural observations on post failure samples have shown a high degree of pore-emanated microcracking (Figure 12a). More definitive conclusions could be drawn using laboratory-determined K_{IC} measurements. However, our analysis may highlight the limit of such micromechanical models, where a complex and heterogeneous microstructure cannot be boiled down to a single parameter such as a mean crack length or mean pore size. Ideally, a new micromechanical model incorporating both microcracks

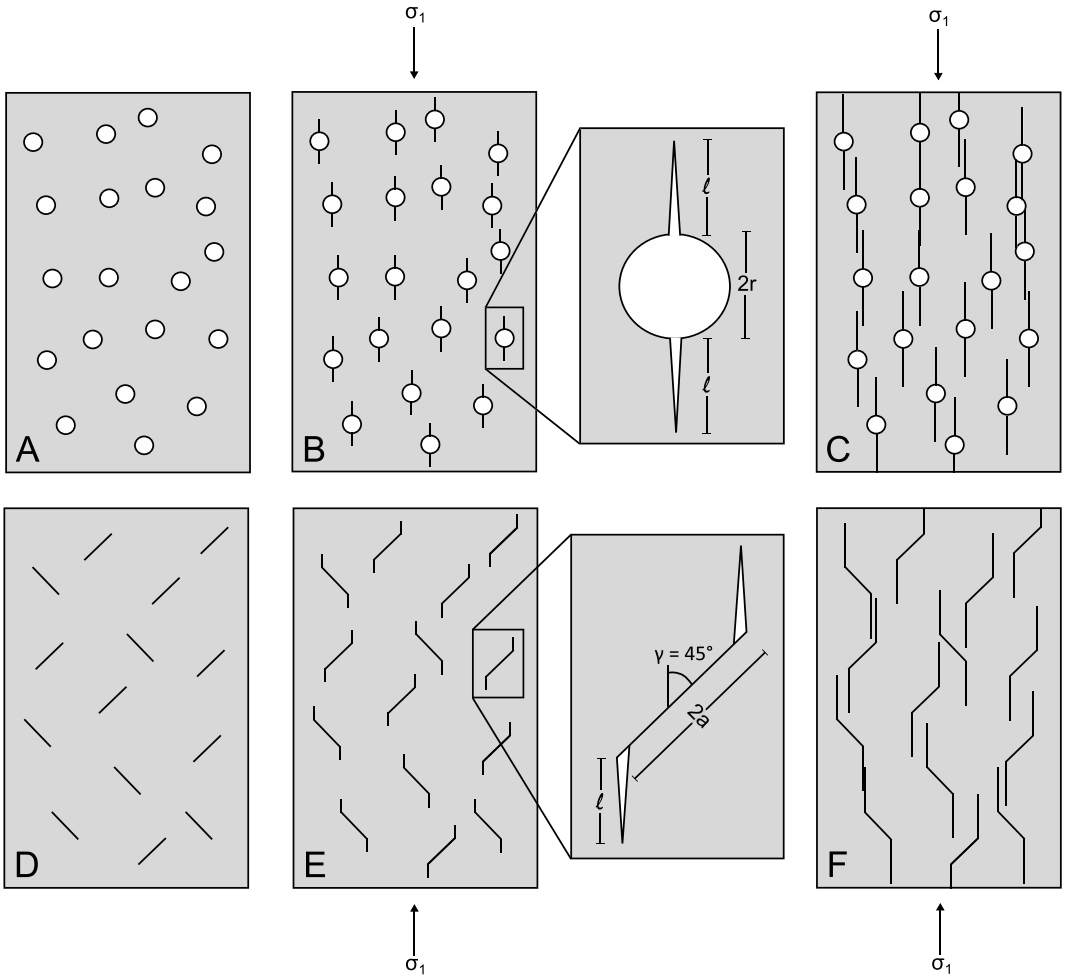

Figure 17. (a) *Sammis and Ashby's* [1986] two-dimensional elastic medium populated by circular holes of uniform radius *r*. (b) Pore-emanated cracks propagate from the pores (to a length *l*) upon the application of an axial stress (one large enough to overcome K_{IC}). (c) Eventually, as axial stress increases, the cracks grow further, interact, and promote macroscopic failure. (d) The sliding wing-crack model [*Horii and Nemat-Nasser*, 1986; *Ashby and Sammis*, 1990; *Kemeny and Cook*, 1991], consisting of a two-dimensional elastic medium populated by cracks of uniform length *2a*. (e) Upon the application of an axial stress (one large enough to overcome the frictional resistance of the crack and the K_{IC}), wing cracks propagate to a length *l*. (f) Eventually, as axial stress increases, the wing cracks grow further, interact, and promote macroscopic failure.

and pores should be developed. While building such a model is beyond the scope of this study, we highlight that this suite of andesites presents an ideal material to formulate such a model.

5.3.2. Geometrical Permeability Modeling: Kozeny-Carman

Permeability models can be grouped into two families, (1) "tube or crack" or statistical permeability models and (2) hydraulic radius or geometrical permeability models where a single equivalent channel is considered [*Guéguen and Palciauskas*, 1994], that are commonly referred to as Kozeny-Carman models. Kozeny-Carman models have been widely used in the earth sciences [e.g. *Paterson*, 1983; *Walsh and Brace*, 1984], due largely to a combination of their simplicity and the fact that the variables can be easily constrained in the laboratory.

The Kozeny-Carman relation has been previously used to model the permeability of volcanic rocks [e.g., *Saar and Manga*, 1999; *Costa*, 2006; *Bernard et al.*, 2007; *Yokoyama and Takeuchi*, 2009]. Several studies have simplified this relation by neglecting variations in element shape (e.g., tube or crack), specific surface area, and tortuosity, instead using an empirically derived constant [*Klug and Cashman*, 1996; *Rust and Cashman*, 2004; *Mueller et al.*, 2005; *Lavallée et al.*, 2013]. While these further assumptions may be somewhat appropriate for rocks with a simple microstructure, such simplification does not adequately pay tribute to the complexity of volcanic rock microstructure. Indeed, even Fontainebleau sandstone suffers void space

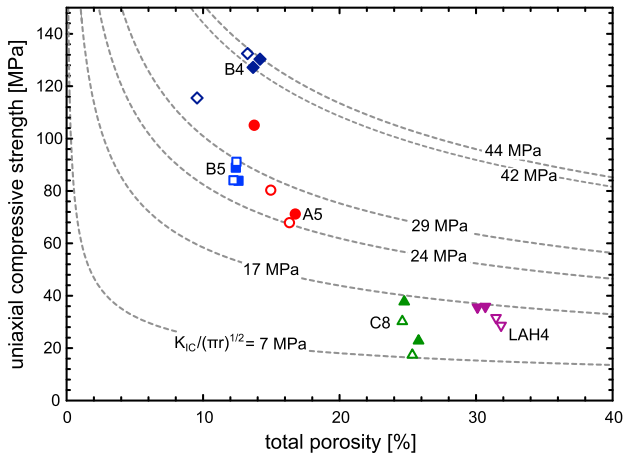

Figure 18. Plot of uniaxial compressive strength against total porosity showing all of the experimental data, together with the theoretical curves from the pore-emanated crack micromechanical modeling (see text for details). Unfilled shapes–as-collected samples; filled shapes–thermally stressed samples.

connectivity issues below 9% porosity [*Bourbié and Zinszner*, 1985]. Further, the use of empirical relations does not permit us to glean information regarding the key factors controlling their fluid transport behavior. Here we take a different approach where we determine the hydraulic radius using Brunauer, Emmett, and Teller (BET) krypton (Kr) adsorption measurements. Krypton adsorption was used as our values for specific surface were approximately at the resolution of nitrogen adsorption. A summary of these data, and the measured water permeability, connected water porosity, and bulk density data, is presented in Table 7. We note that the specific surface of sample B5 is much higher than the other andesites and likely reflects the fact that B5 contains a much greater proportion of small vesicles (Figures 6 and 7).

The Kozeny-Carman relation is of the form

$$k_{KC} = \frac{\varphi (r_H)^2}{b\tau^2} \tag{6}$$

where k_{KC} is the permeability, φ is the connected porosity, b is a geometrical factor, τ is the tortuosity of the flow channel (i.e., the ratio of its actual to nominal length), and r_H is the hydraulic radius. The hydraulic radius can be defined as follows:

$$r_H = \frac{V_{pores}}{S_{pores}} \tag{7}$$

where V_{pores} is the volume of pores and S_{pores} is the surface of the pores. The specific surface area of the connected pore space inside a rock can be determined using BET krypton adsorption. This technique can be used to determine the hydraulic radius:

$$r_H = \frac{\varphi}{\rho_b S_{BET}} \tag{8}$$

where ρ_b is the bulk density and S_{BET} is the specific surface area as determined by BET. The Kozeny-Carman relation can therefore be recast as

$$k_{KC} = \frac{\varphi^3}{b\tau^2 \rho_b{}^2 S_{BET}{}^2} \tag{9}$$

Table 7. Data Summary for the Andesite Samples Used for the Permeability Measurements and Modeling

Connected Water Porosity (%)	Sample	Water Permeability (m^2)	Bulk Density (kg/m^3)	Specific Surface Area S_{BET} (m^2/kg)	Tortuosity Assuming Cracks ($b = 12$)
7.4	B5-5	3.61×10^{-17}	2474.64	100	3.9
8.2	B4-2	3.59×10^{-17}	2443.04	26	17.8
9.2	A5-11	1.09×10^{-16}	2446.08	15	21.0
9.6	A5-1	3.62×10^{-16}	2403.23	16	11.7
11.9	A5-7	5.45×10^{-14}	2317.94	20	1.1
15.2	C8-9	1.15×10^{-13}	2188.72	35	2.3
15.5	C8-8	4.57×10^{-13}	2127.07	28	0.4
23.8	LAH4-9	5.65×10^{-13}	1971.65	57	0.4
23.8	LAH4-7	6.96×10^{-13}	1998.97	51	0.4

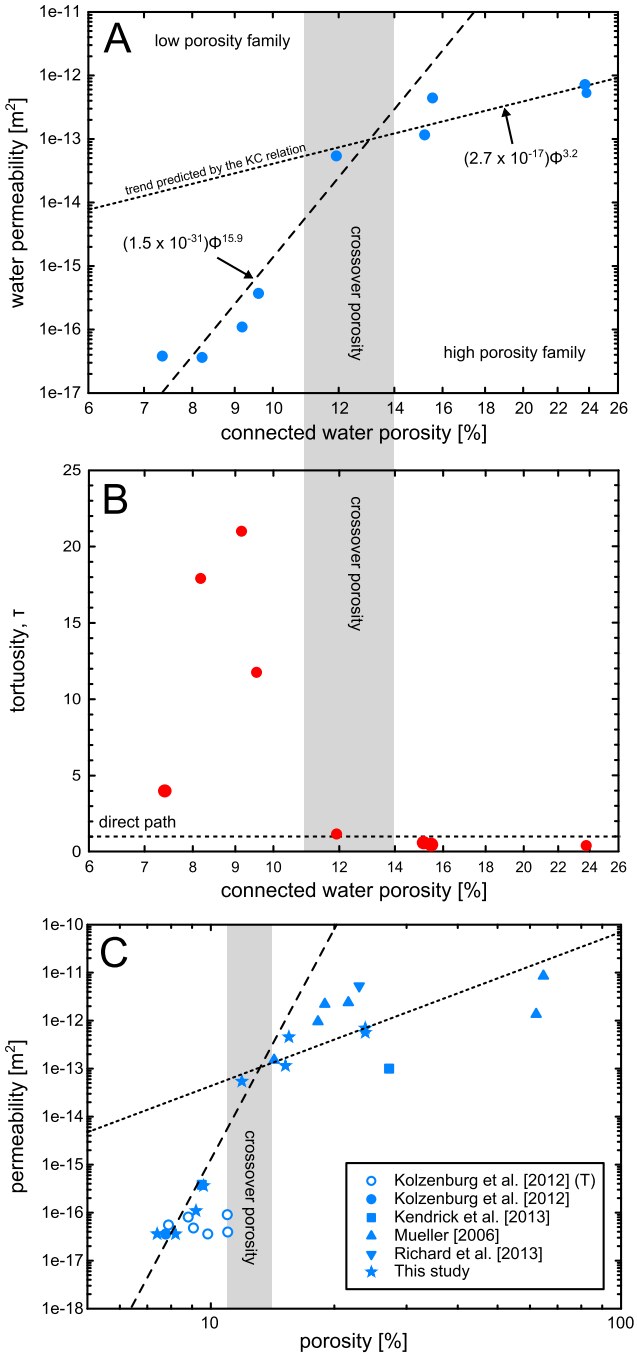

Figure 19. (a) Log-log plot of water permeability against connected water porosity. The dashed and dotted lines are the best fit trends for the low-porosity family (steep curve) and the high-porosity family (shallow curve), respectively. Both lines are accompanied by their power law exponent. The "crossover porosity" (11–14%), where the two trends meet, is shaded in grey. (b) Log-linear plot of tortuosity against connected water porosity. The crossover porosity range (11–14%) is shaded in grey. (c) Permeability against porosity for rocks from Volcán de Colima, plotted on log-log axes. The *Kolzenburg et al.* [2012] and the *Kendrick et al.* [2013] data are water permeabilities measured on andesitic rocks under a confining pressure of 5 MPa and a pore fluid pressure gradient of 1 MPa. (T)–samples that contain healed tuffisites. The *Mueller* [2006] data are gas (argon) permeabilities measured under a confining pressure of 0 MPa using the pulse decay method (2.5 MPa on one side and 0 MPa on the other). The low-porosity samples of *Mueller* [2006] were performed on lava samples from the 1999 block-and-ash flow deposit, and the high-porosity samples were pumiceous samples from the 1913 eruption. The *Richard et al.* [2013] datum is for a sample collected from the 1999 block-and-ash flow deposits; gas (argon) permeability was measured under a confining pressure of 0 MPa using the pulse decay method (4 MPa on one side and 0 MPa on the other). The dashed and dotted lines are the power law trends shown in Figure 19a. The crossover porosity range (11–14%) is shaded in grey.

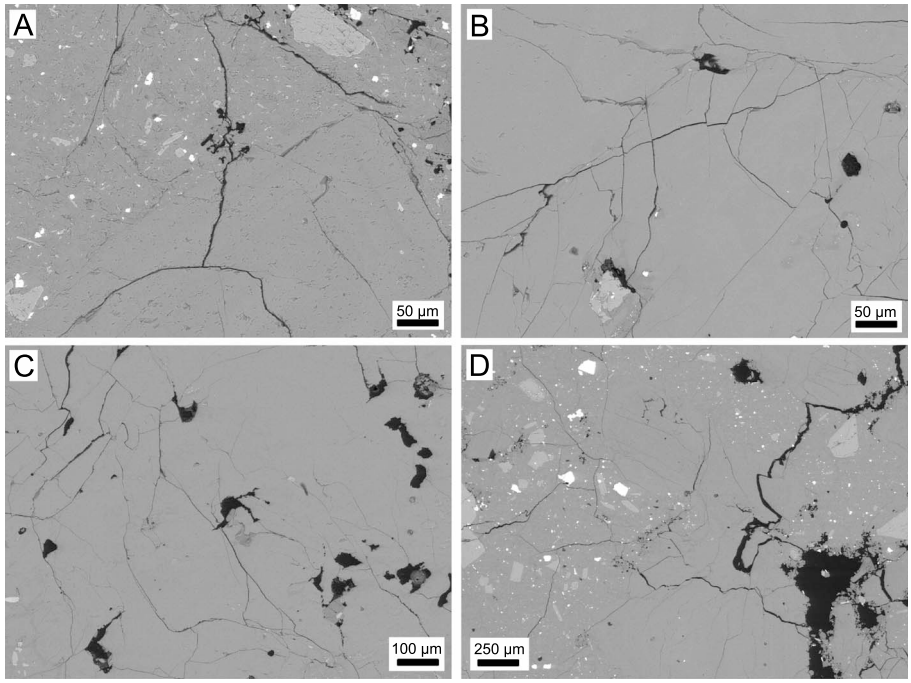

Figure 20. Scanning electron microscope photographs of an as-collected sample of B5 highlighting the tortuous nature of the microcracking.

We find the power law exponent for our high-porosity (15–24%) andesites to be close to 3 (Figure 19a), a value in agreement with the Kozeny-Carman model [see *Bourbié and Zinszner*, 1985; *Doyen*, 1988]. In detail, one would expect a power law exponent of 3 if the elements controlling the permeability are cracks [*Guéguen and Palciauskas*, 1994]. For this range of porosities, we can assume that the tortuosity and the specific surface area are largely independent of the porosity (a power law exponent of 3 is indicative of this independency). In theory, if these microstructural parameters remained unchanged when the porosity is reduced, samples of lower porosity should follow the same trend (the dotted line on Figure 19a). This is however not the case (i.e., one or more of the parameters is changing as porosity is reduced). The power law exponent for the low-porosity (8–12%) samples is much larger (about 16) and can be explained in terms of a dramatic reduction in void space connectivity which, in turn, results in a significant increase in tortuosity below the crossover porosity (11–14%). We note that crossover porosity for the andesites is only slightly higher than that for Fontainebleau sandstone (about 9%) [*Bourbié and Zinszner*, 1985].

Microstructurally, the crossover porosity (Figure 19) in the andesites is likely to represent a critical vesicle content (a combination of vesicle size and density) that efficiently connects the microcrack population and allows the water to travel a much more direct path through the sample, rather than restricting flow to long and tortuous microcracks. Indeed, SEM analysis of one of the low-porosity andesites aptly demonstrates the convoluted path the water must take to pass through the sample; the SEM photographs show "cross roads," "dead ends," and multiple pathways for fluid flow (Figure 20).

Although it is clear that no single Kozeny-Carman relationship will be able to describe the full suite of data, we can use the model to support our hypothesis by estimating values for the tortuosity, τ. Using our experimentally determined values for water permeability, BET specific surface area, density, and porosity (Table 7), we can solve equation (9) to find values for the unknown term $b\tau^2$. Values for geometrical factor b can vary [*Bernabé et al.*, 2003], but it can be assumed that $b = 8$ if the transport elements are "tubelike" and $b = 12$ if they are "crack-like" [*Bernabé et al.*, 2010]. Since cracks are controlling the permeability of the andesites of this study (the power law exponent is 3) [see *Guéguen and Palciauskas*, 1994], we will assume that $b = 12$ and solve for τ. Values for τ are commonly between 1 (direct path) and 3 [*Dullien*, 1979]. We find that, when $b = 12$, τ ranges from 0.4 to 21.0 (Table 7). Values of τ for each sample, for a constant value of b (12 in this case), are plotted against porosity in Figure 19b. Figure 19b shows that there is a large increase in tortuosity

below the crossover porosity. We find τ values below 1 above the crossover porosity and values almost 20 below the crossover porosity (such high values of tortuosity are not uncommon for volcanic rocks) [see *Wright et al.*, 2009]. While we note that values of τ below 1 are impossible (true values likely to be close to, albeit higher, than 1), we emphasize the striking difference in tortuosity above and below the crossover porosity. This analysis supports our initial conjecture that the deviation from Kozeny-Carman behavior is related to inefficient element connectivity and high tortuosity in the samples below a porosity of about 12%. A similar interpretation may explain the low permeabilities of the rhyolite and obsidian samples of *Eichelberger et al.* [1986] below 60% porosity. Our data are plotted alongside previously published permeability data for rocks from Volcán de Colima (Figure 19c). This compilation plot shows that our power law trends and the position of the crossover porosity are in agreement with the available published data.

To conclude we would like to highlight that, even using samples from the same volcano with an identical chemical composition, understanding their permeability still remains a challenge. We suggest that a deviation from Kozeny-Carman behavior may exist in other extrusive volcanic rocks that contain a combination of vesicles and microcracks. We implore that the complex controls on permeability in volcanic rocks require a deeper understanding. Further discussion on the implications of these permeability data can be found in section 5.5.

5.4. The Influence of Thermal Stressing on Andesites From Volcán de Colima

Our AE analysis suggests that the onset temperature and the extent of thermal microcracking differed greatly between the samples, perhaps reflecting the broad crystal size distribution, crystal/glass fraction, and porosity of volcanic rocks. Volcanic rocks often have a heterogeneous (often bimodal) crystal size distribution and may therefore react to thermal stressing in a different way to granites or sandstones. *Tang et al.* [2011] stress the importance of crack propagation at the mortar/coarse aggregate interface in heterogeneous concrete, somewhat analogous to the groundmass/phenocryst interface in volcanic rocks. We also observed that, for some of the andesites of this study, thermal microcracking was more prevalent during the cooling stage of the thermal stressing experiment (Figure 14). While previous studies largely attribute thermal microcracks as the result of thermal expansion mismatches between minerals, our study highlights that the thermal contraction of minerals can also be important. While data on this phenomenon in rocks are rare, it has been previously observed in studies on porcelain [*Kirchhoff et al.*, 1982] and concrete [*Heap et al.*, 2013].

Stereological microcrack analysis provided lower microcrack densities and a higher anisotropy for the samples thermally stressed to 450°C. We do not suggest that thermal stressing has reduced the microcrack density or changed the anisotropy of the andesite samples. This difference is likely due to the fact that the counting did not take place on the same sample, i.e., both before and after thermal stressing (as was the case for the physical properties described above and listed in Table 4). We must conclude that the thermal microcracking that took place in our samples was much less than the natural variability between samples taken from the same block of material. Unfortunately, no firm conclusions can be drawn from such stereological techniques for the studied materials. We observed modest changes in rock physical properties as a result of thermal stressing. We saw a modest increase in connected porosity, and modest decreases in ultrasonic wave velocities and dynamic elastic moduli. This can be interpreted as a result of a small increase in the already extensive thermal microcrack network, as evidenced by the output of AE during our thermal stressing experiments.

Thermal microcracking has been previously shown to induce changes to the physical properties of rocks [e.g., *David et al.*, 1999]. However, few studies have investigated the propensity of volcanic rocks to develop thermal microcracks and their consequences on rock physical properties [*Jones et al.*, 1997; *Lebedev and Kern*, 1999; *Vinciguerra et al.*, 2005; *Heap et al.*, 2009; *Smith et al.*, 2009; *Nara et al.*, 2011]. In general, the influence of thermal stressing on the physical properties of volcanic rocks is not so clear. In the case of a basaltic lava deposit from Mount Etna, the permeability, elastic wave velocities [*Vinciguerra et al.*, 2005], and elastic moduli [*Heap et al.*, 2009] remained unchanged after exposure to 900°C. Similarly, *Smith et al.* [2009], in triaxial experiments on an andesite from Mount Shasta (California, USA), found that, at in situ temperatures from 25 to 600°C, the static Young's modulus of their andesites remained constant. However, some studies report large thermally induced physical property modifications for volcanic rocks. For an aphyric basalt from Iceland, *Jones et al.* [1997] showed that thermal stressing increases the permeability above temperatures of 300°C (later reinforced by *Nara et al.* [2011]), and *Vinciguerra et al.* [2005] showed that its *P* wave velocity was

reduced from 5.2 to 4.0 km s^{-1} upon exposure to 900°C. What we can conclude from this incomplete data set is that, in the absence of mineralogical changes, aphyric (or low porosity) volcanic rocks appear more susceptible to thermal microcracking than porphyritic volcanic rocks, a conclusion also surmised by *Jones et al.* [1997]. It is also possible that the immunity of some materials to further thermal microcracking is linked to the presence of a preexisting thermal microcrack network (i.e., materials that have already undergone one or more heating/cooling episodes), a concept linked to the Kaiser "temperature-memory" effect [*Yong and Wang*, 1980]. This interpretation has been previously proposed for the highly microcracked basalt from Mount Etna [*Vinciguerra et al.*, 2005; *Heap et al.*, 2009].

The data from our study suggest that thermal stressing to 450°C does not influence the UCS of our suite of andesite samples. While we can cite that natural variability could again obscure any observable difference in UCS (as-collected and thermally stressed UCS cannot be measured on the same sample), the influence of thermal stressing on the strength of materials, as portrayed throughout the literature, is unclear. Some materials weaken as a result of thermal microcracking (e.g., granites) [*Homand-Etienne and Houpert*, 1989], and others weaken as a result of chemical changes (e.g., tuffs) [*Heap et al.*, 2012]. However, in some materials (largely of volcanic origin), no weakening was observed over a wide range of temperature [*Bauer et al.*, 1981; *Meredith et al.*, 2005; *Balme et al.*, 2004; *Heap et al.*, 2009; *Smith et al.*, 2009], even though the rocks host an abundance of feldspars (feldspars have an extremely anisotropic thermal expansion coefficient) [see *Tribaudino et al.*, 2010]. For example, the UCS of a basaltic lava deposit from Mount Etna did not decrease after exposure to 900°C [*Heap et al.*, 2009] and can be explained by the fact that this material appears to resist further thermal microcracking, as evidenced by its unchanged *P* wave velocity after exposure to 900°C [*Vinciguerra et al.*, 2005]. However, in the case of the aphyric basalt from Iceland (porosity = 4.5%), the *P* wave velocity was reduced from 5.2 to 4.0 km s^{-1} [*Vinciguerra et al.*, 2005] upon exposure to 900°C but its UCS and indirect tensile strength were unaffected [*Meredith et al.*, 2005]. Another study found that high in situ temperatures had little impact on fracture toughness of basaltic lava deposits from Mount Etna and Vesuvius [*Balme et al.*, 2004] and the compressive strength of andesite [*Bauer et al.*, 1981; *Smith et al.*, 2009]. From these observations we can conclude that, if a volcanic rock is exposed to thermal stressing, it does not necessarily change the most deleterious microcrack (i.e., new thermal microcracks are relatively small), which plays a large role in failure in compression. However, and owing to the paucity of data, we conclude that a complete picture of the effect of thermal stressing on volcanic rocks does not exist to date. We suggest that thermal stressing (on short timescales) does not significantly modify the andesites due to a combination of (1) the stability of its mineral phases, (2) the presence of a preexisting pervasive thermal microcrack network, (3) their porphyritic texture, and (4) their high porosities (i.e., the thermal expansion of the minerals could simply be accommodated by the porosity).

5.5. Volcanological Implications

The main goal of this study was to characterize the microstructural, physical, and mechanical properties for a representative range of andesitic rocks that form the volcanic edifice at Volcán de Colima. Our findings demonstrate that the physical and mechanical properties of these volcanic rocks are strongly controlled by their microstructure. The andesitic rocks from Volcán de Colima are intensely fractured, a result of their relatively fast cooling history, and contain high vesicle densities and a wide vesicle size distribution. As a result they have high porosities and permeabilities and low bulk densities, elastic wave velocities, Young's moduli, and compressive strengths. The nature of volcanic rock formation, combined with the relatively unstable conditions in which they exist, suggests that this is may be the case for many volcanic rocks. The wide range of microstructural, physical, and mechanical properties exhibited by this representative suite of andesites highlights the heterogeneous nature of the rocks comprising the edifice at Volcán de Colima. Although it may appear counterintuitive, stratovolcanoes constructed from rock strata with vastly different physical and mechanical properties may be "stronger" as a result. Layers of rock with different Young's moduli and strengths impact the distribution of stress and strain and can promote the deflection or arrest of propagating dykes and fractures at the contacts between layers [*Gudmundsson*, 2011], thus increasing the amount of strain energy required for large-scale edifice failure [*Gudmundsson*, 2012].

Due to the sensitivity of elastic waves to microcracks, an increase in microcracking (due to thermal or mechanical stresses) and/or the movement of fluids within a region of the volcanic edifice hosting highly microcracked rocks could alter seismic velocities at Volcán de Colima. We suggest that such findings should

be considered in tomographic, seismic data inversion of subvolcanic structures, and V_p/V_s anomaly analysis. Knowledge of the elastic moduli for representative volcanic rock is important for (1) the reliable modeling of the ground deformation at volcano edifices [e.g., *Manconi et al.*, 2007, 2010], (2) the calibration of damage mechanics criteria and the development of appropriate time-to-failure laws [e.g., *Voight*, 1989; *Kilburn*, 2003; *Kilburn and Sammonds*, 2005], and (3) the distribution of stress and strain and the understanding of the propagation and arrest and fractures and dykes [e.g., *Gudmundsson*, 2011], amongst many more. All require a robust knowledge of the elastic moduli of the representative rocks and their modification under mechanical and thermal stresses. The heterogeneous nature of the rocks comprising the edifice at Volcán de Colima highlights that the currently common assumption of rock homogeneity in volcano modeling is an oversimplification that can lead to misinterpretations of derived source (e.g., a magma chamber, a zone of overpressurized fluids, or a combination of the two) parameters [*Manconi et al.*, 2007, 2010]. Previously, ground deformation [*Murray and Ramírez Ruiz*, 2002; *Murray and Wooller*, 2002; *Pinel et al.*, 2011] and viscoelastic [*De la Cruz-Reyna and Reyes-Davila*, 2001] modeling have been employed as forecasting tools at Volcán de Colima. For instance, *Pinel et al.* [2011] used a Young's modulus of 3 MPa and, although they remark that this value is very low compared to previously published values for rock, perhaps (when one accounts for the fact that laboratory Young's modulus measurements exclude macroscopic fractures; laboratory measurements are commonly 1.5–5 times greater than the in situ modulus of the same rock) [*Gudmundsson*, 2011] their estimate is not so unrealistic, as evidenced by the low values of Young's moduli obtained in this study. We suggest (1) that low values of Young's modulus should be considered when choosing the parameters for the modeling of unrest phenomena and (2) that the assumption of rock homogeneity is an oversimplification at andesitic stratovolcanoes. Further, we highlight that recent finite element modeling [*Manconi et al.*, 2010] and experimental studies [*Heap et al.*, 2009, 2014] suggest that the static values may be more appropriate in volcanic hazard modeling.

The ease at which exsolved gases can escape from rising magma during periods of unrest can have drastic consequences on the eruption style: effusive or explosive [*Woods and Koyaguchi*, 1994]. The permeability of magma, and the surrounding host rock, is therefore of crucial importance. For magma, the percolation threshold is likely to represent an abrupt transition between essentially zero permeability to reasonably high permeability. Above the percolation threshold for magma, exsolved gas can escape vertically but can also escape horizontally, assuming a lateral connection of bubbles and a permeable host rock. We also speculate that the gas in bubbles on the outermost edges of the conduit (i.e., in contact with the host rock) could escape below the percolation threshold for magma. While a variety of studies discuss magma permeability using data from explosive or effusive volcanic products, we stress that we consider our permeability measurements as representative of the host (country and wall) rock, not the magma in the conduit. However, and as discussed above, we consider that host rock permeability is likely to play an important role in shaping eruption characteristics [see also *Jaupart*, 1998]. We have shown that the host rock can be very permeable ($\sim 10^{-13}$ m^2, i.e., similar to magma permeability estimates above the percolation threshold) and could therefore allow significant horizontal gas loss, reducing the potential for large explosive eruptions. Evidence for host rock gas transport include the following: (1) lava close to the conduit wall can be devoid of vesicles, suggesting efficient gas escape [*Jaupart*, 1998] and (2) the presence of tuffisites [*Stasiuk et al.*, 1996; *Tuffen et al.*, 2003, and references therein] that are extremely common at Volcán de Colima [*Kolzenburg et al.*, 2012]. Further, it is likely that lateral permeability may be preferentially enhanced by microcracking within the magma at the conduit boundary [*Laumonier et al.*, 2011; *Lavallée et al.*, 2013; *Plail et al.*, 2014]. "Hydrofracturing," due to rising pore pressures inside the host rock, could further increase the microcrack density and permeability of the adjacent host rock [*Caricchi et al.*, 2011]. We suggest that horizontal gas escape should be considered in volcanic permeability models at Volcán de Colima and at other stratovolcanoes worldwide.

Another goal of this study was to make some of the first steps in understanding the micromechanical processes responsible for the deformation of volcanic rocks and to revisit the potential of geometrical permeability models. A deeper understanding of the micromechanics of edifice-forming volcanic rocks, and the physics underpinning their permeability, allows for a better assessment of volcano hazards [e.g., *Jaupart*, 1998; *Costa et al.*, 2009]. Previous studies have shown that the pore-emanated crack model can adequately describe the mechanical behavior of porous tuffs [*Zhu et al.*, 2011] and bubbly magma [*Vasseur et al.*, 2013].

Perhaps this is not surprising since the microcrack density for such materials is usually very low (in other words, the porosity consists of vesicles only). However, for lava deposits, where microcracks and vesicles are both abundant, both microstructural elements contribute to their deformation (since pore-emanated or wing-crack modeling could not capture the mechanics). Unfortunately, no model that combines both elements exists. We envisage that future work on the micromechanics of volcanic rocks, including the formation of a multielement model, will help unravel their complex micromechanics and provide vital information for volcanic hazard assessment. While permeability models (such as Kozeny-Carman) have been adopted for volcanic rocks [*Costa*, 2006], the validity of empirically derived relationships between porosity and permeability is questionable due to their heterogeneity (even those from the same eruption). We found that Kozeny-Carman permeability modeling does not accurately capture the fluid flow properties of the andesites of this study. While other statistical permeability models are available, and should be the focus of future studies, we anticipate that understanding fluid flow will certainly represent a challenge for volcanic materials.

This study has shown that, on short timescales, thermal stressing will not significantly weaken the edifice-forming andesites at Volcán de Colima and therefore the edifice as a whole. However, we should emphasize that the heating/cooling rates used in this study were perhaps high when compared with heating/cooling rates in nature. Prolonged deformation at higher temperatures could provide the time needed for the chemical alteration of unstable mineralogical assemblages or for healing, providing that the deformation timescale exceeds the time required for the structural relaxation of the interstitial melt phase [e.g., *Tuffen et al.*, 2003]. We suggest that, for a deeper understanding of the influence of thermal stressing, further experimentation using longer timescales is required.

6. Conclusions

1. Our study has shown that a representative suite of andesites from Volcán de Colima is pervasively microcracked and has high vesicle densities and a wide vesicle size distribution. Due to the isotropic nature of this microcracking (and the origin of the samples), we suggest that the microcracks are predominantly of thermal origin and formed as a result of rapid cooling. Since microcrack densities are similar (their cooling histories are therefore likely to be similar), the large differences in porosity are the result of varying vesicle size and density.
2. The complex microstructure (i.e., microcracks and vesicles) of these andesites has left them with high porosities and permeabilities and low densities, elastic wave velocities, Young's moduli, and compressive strengths.
3. The wide range of microstructural, physical, and mechanical properties exhibited by this representative suite of andesites highlights the heterogeneous nature of the rocks comprising the edifice at Volcán de Colima.
4. Micromechanical modeling (pore-emanated crack versus sliding wing-crack modeling), implemented to decipher the micromechanical controls on deformation, was unable to accurately capture the micromechanics of the tested andesites, due to their microstructural complexity. These analyses highlight the need for a micromechanical model that combines both microcracks and vesicles. We suggest that these andesites are an ideal material to formulate such a model.
5. A unique Kozeny-Carman permeability model does not exist for the studied suite of andesites. Two families exist that can be distinguished by their void space connectivity and tortuosity. Below the crossover porosity, flow occurs mainly through highly tortuous microcracks. Above the crossover porosity, the fluid pathways are simplified by an increasing vesicle content (a combination of size and density). These analyses highlight that understanding the permeability of volcanic rocks still remains a challenge and requires a deeper understanding.
6. We found that thermally stressing these andesites to 450°C slightly increases their porosities and slightly decreases their elastic wave velocities and dynamic elastic moduli. This is interpreted as the result of a small increase in the already extensive microcrack network, as evidenced by the output of AE during thermal stressing. We suggest that thermal stressing (on short timescales) does not significantly modify the andesites due to a combination of (1) the stability of its mineral phases, (2) the presence of a preexisting pervasive thermal microcrack network, (3) their porphyritic texture, and (4) their high porosities (i.e., the thermal expansion of the minerals is simply accommodated by the porosity).

7. Thermal stressing to 450°C does not influence the UCS of the andesite samples (within the expected natural variability of the tested samples). We interpret that thermal stressing does not change the most deleterious microcrack, which plays a large role in failure in compression.
8. We suggest that our findings should be considered in (1) edifice stability assessment, (2) the interpretation of volcano seismic tomography and V_p/V_s anomaly analysis, (3) the modeling of unrest phenomena at andesitic stratovolcanoes, and (4) assessing the potential contribution of the host rock in magma degassing.

Appendix A: Additional Methods

A1. Microstructural Characterization

For both analyses, photomicrograph maps of each sample were collated using an optical microscope under transmitted fluorescent light. The maps were then converted to binary images. In this study we refer to microcracks and vesicles. Both are void space within the rock. While there is a clear difference in genesis between the two microstructural features, they were differentiated in thin section by their aspect ratio. The aspect ratio of a microcrack is typically above 1:100. Vesicles typically range from 1:1 (a perfect circle) down to 1:10. We note that these analyses represent only the connected microstructural elements (i.e., those impregnated with the fluorescent epoxy).

A1.1. Microcrack Analysis

The two-dimensional "connected" microcrack surface area S_v for each sample was measured by counting perpendicular $(P_L)_I$ and parallel $(P_L)_{II}$ microcrack intercepts within an $11 \times 11\,mm^2$ grid, containing both horizontal and vertical lines spaced by 0.1 mm (Figure A1) [*Underwood*, 1970; *Wu et al.*, 2000]. The method provides the microcrack density in two orthogonal directions within the studied plane.

A complementary assessment of the microcrack anisotropy was performed using the modified Cantor-dust method [*Volland and Kruhl*, 2004] included in the automated pattern quantification toolbox AMOCADO [*Gerik and Kruhl*, 2009]. In detail, a set of 260 to 420 parallel lines (spaced by three pixels; equivalent to percentage rate of the radius) was superimposed onto a circular 1–1.5 cm^2 area of the binary images, and the number of segments $N(s)$ of length s that covers the microcrack-line intercept was plotted cumulatively versus the corresponding segment length on a log-log diagram. The threshold for the detection of a microcrack intercepted by a scan line was set to a length of three pixels. The data points in the cumulative segment-length plot formed a straight line (i.e., exponential distribution), and the slope calculated by the linear regression (excluding the 5% end tails of the data sets) provided a size distribution coefficient. From its initial horizontal position, the set of scan lines were subsequently rotated counterclockwise stepwise by an angle of 1° around the center point and the procedure was repeated up to an angle of rotation $\Sigma\omega < 180°$ (due to the rotational symmetry of the scan lines). All computed slope values were plotted in a direction versus slope diagram and approximated with a best fit ellipse. Analyses of anisotropic complex patterns (long axis to short axis ratio) yield oriented ellipses as best fits to the data point distributions.

A1.2. Vesicle Analysis

Two-dimensional connected vesicle area, density, circularity, aspect ratio, and roundness were determined using ImageJ. For these analyses, the binary images were further thresholded to select only the vesicles (Figure A1). The above vesicle parameters were automatically calculated using ImageJ using the following formulae:

$$\text{circularity} = 4\pi\left(\frac{\text{area}}{[\text{perimeter}]^2}\right) \tag{A1}$$

$$\text{aspect ratio} = \frac{\text{major axis}}{\text{minor axis}} \tag{A2}$$

$$\text{roundness} = 4\left(\frac{\text{area}}{\pi(\text{major axis})^2}\right) \tag{A3}$$

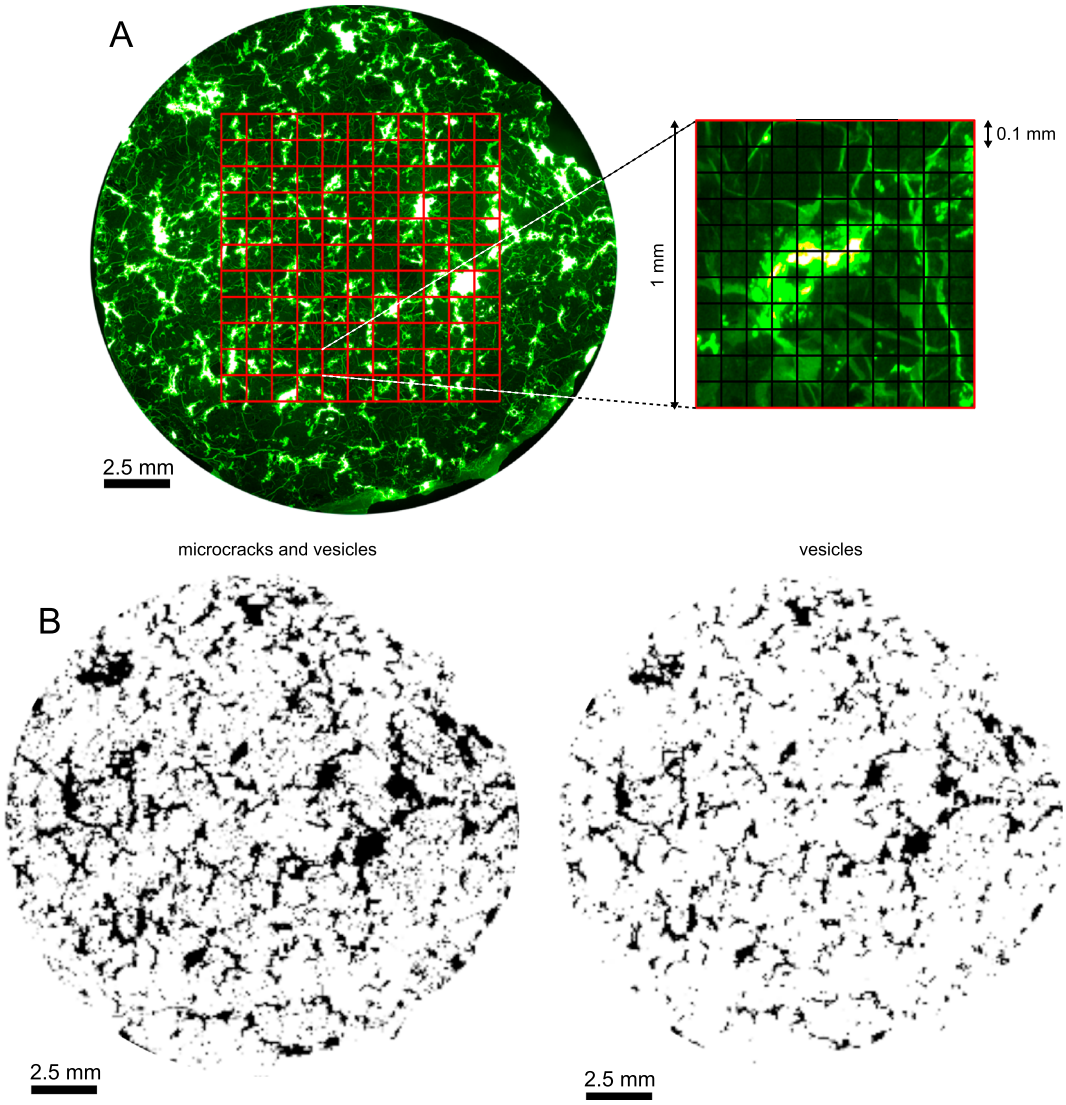

Figure A1. Diagrams outlining the two-dimensional stereological method for counting perpendicular $(P_L)_I$ and parallel $(P_L)_{II}$ microcrack intercepts within an 11 × 11 mm^2 grid containing both horizontal and vertical lines spaced by 0.1 mm [see *Underwood*, 1970].

The equivalent vesicle radii were then determined, assuming circular vesicles and using the following formula:

$$\text{equivalent vesicle radius} = \sqrt{\frac{\text{area}}{\pi}} \tag{A4}$$

A.2. Connected and Total Porosities

The connected water porosities of the samples were measured using the triple-weight water saturation (distilled water) method, using Archimedes' principal [see *Guéguen and Palciauskas*, 1994]:

$$\varphi_w = \frac{m_2 - m_1}{m_2 - m_3} \tag{A5}$$

where m_1, m_2, and m_3 are the dry mass (vacuum dried at 40°C for at least 24 h), saturated mass (saturated with distilled water under a vacuum), and saturated submerged mass, respectively. Powdered skeletal densities

Table A1. Powdered Skeletal Densities for Each of the Five Blocks of Andesite

Block	Powdered Skeletal Density, ρ_{s_p} (kg m^3)
B5	2738.1
B4	2712.8
A5	2729.3
C8	2679.1
LAH4	2737.5

ρ_{s_p} were measured using a helium pycnometer (AccuPyc II 1340) using Boyle's law (Table A1). Total φ_t porosities were then calculated using the following formulae:

$$\varphi_t = 1 - \frac{\rho_b}{\rho_{s_p}} \tag{A6}$$

where ρ_b is the bulk sample density.

Water and total porosities were measured on many core samples from each of the five blocks of andesite. First, this provides insight into the variability of the materials. Second, in order to be able to compare the mechanical data of samples from the same block, we used these data to select core samples of similar porosities. Third, we were interested in sampling a range of porosities for our permeability measurements.

A3. Elastic Wave Velocities

The measurements were all performed (at the Laboratoire de Déformation des Roches, Strasbourg, Figure A2) using a device coupling: (1) a digital oscilloscope (Agilent Technologies DSO5012A digital storage oscilloscope), (2) a waveform pulse generator (Agilent Technologies 33210A, 10 MHz function/waveform generator), (3) two piezoelectric transducers, located within steel endcaps at the top and bottom of the sample, with a resonant frequency up to 1 MHz, (4) a load cell, and (5) a signal amplifier. Samples were held in the device at a constant contact force of 600 N (equating to a stress of about 1.9 MPa) to ensure the adequate transmission of the signal between the endcaps and the sample and to ensure reproducibility between one measurement and the next. In the case of sample material LAH4 (the sample with the highest porosity), a force of 200 N (about 0.6 MPa) was chosen to avoid inducing any damage. The frequency of generated signal was set at 700 kHz for *P* waves and 300 kHz for *S* waves.

Elastic wave velocities were subsequently used to calculate the dynamic Young's modulus E_d and the dynamic Poisson's ratio v_d using the following formulae:

$$E_d = \rho_b \frac{V_s^2\left(3V_p^2 - 4V_s^2\right)}{V_p^2 - V_s^2} \tag{A7}$$

$$v_d = \frac{V_p^2 - 2V_s^2}{2\left(V_p^2 - V_s^2\right)} \tag{A8}$$

where ρ_b is the bulk sample density and V_p and V_s are the *P* wave and *S* wave velocities, respectively.

The tangent moduli or static Young's moduli E_s were calculated using the stress-strain data collected during the unconfined compressive strength (UCS) experiments. First, each stress-strain curve was fitted with a third-order polynomial. The resultant equations were then differentiated and the tangent modulus (i.e., the Young's modulus) was determined over their entire lengths. We take the Young's modulus from the region where the moduli did not change (corresponding to the maximum slope) [e.g., see *Heap and Faulkner*, 2008]. The axial stress at the region of maximum slope varied from sample to sample (typically between 15 and 100 MPa). We note that this only represents one Young's modulus in a deforming rock sample, since the elastic moduli will be developing in an anisotropic manner.

A4. Permeability Measurements

Water (distilled water) permeability measurements were made in a hydrostatic pressure vessel (at the Laboratoire de Déformation des Roches, Strasbourg, Figure A2) along the long axis of the cylindrical samples (i.e., the *Z* direction). Permeabilities were measured for a suite of samples that best covers the observed range of connected water porosities (from 7.4 to 23.8%). All measurements were collected under ambient laboratory temperatures. Prior to experimentation the samples were vacuum saturated with distilled water. The measured sample was then inserted into a viton jacket, placed between two steel endcaps, and lowered into the pressure vessel. A confining pressure (provided by distilled water) of 2 MPa was then applied to the sample. Water permeability was measured using the steady state flow method where the differential pore pressure ($P_{up} - P_{down}$) was kept constant (0.5 MPa). The flow rate *Q* was measured at the downstream side of

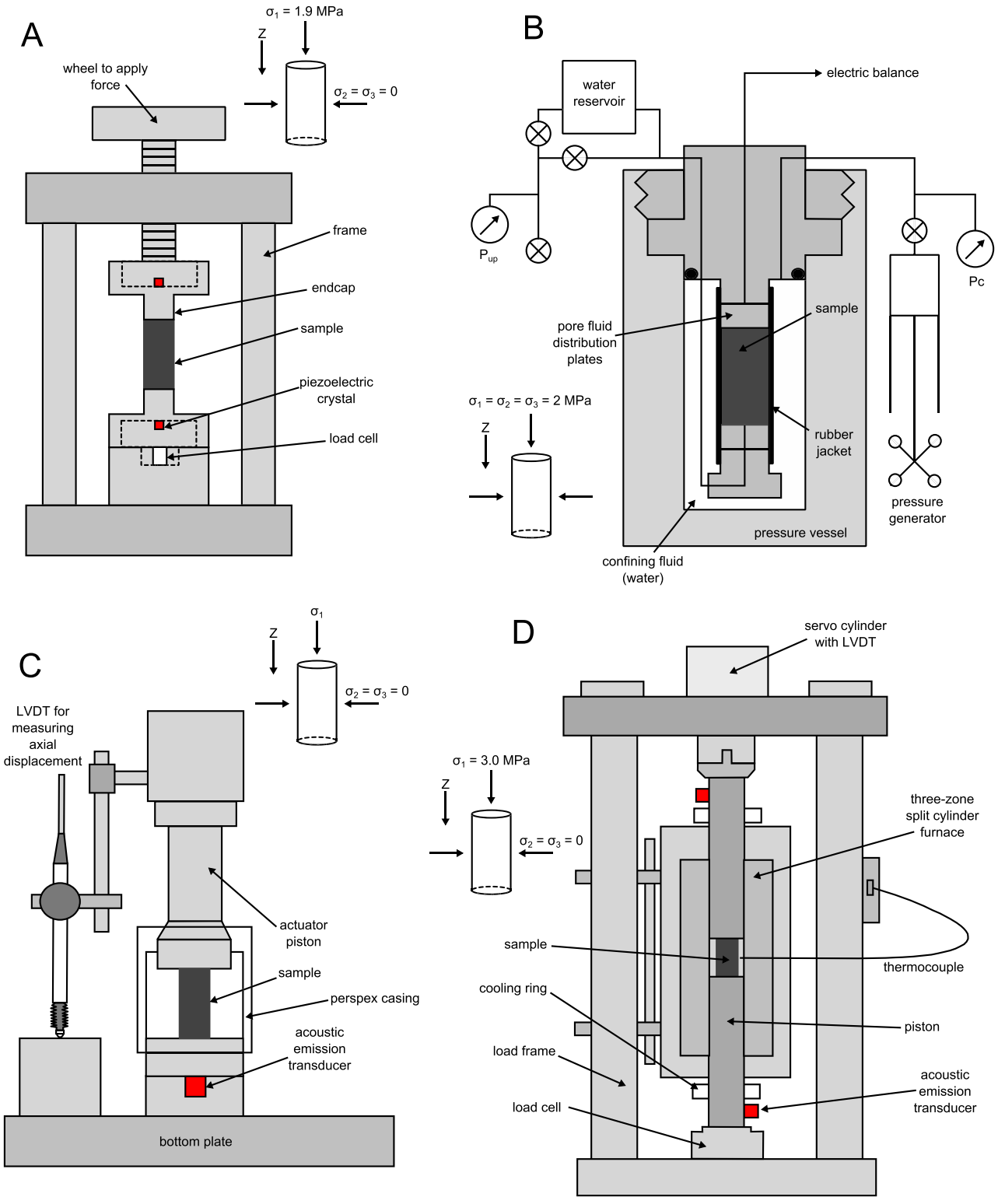

Figure A2. (a) Schematic diagram of the experimental arrangement used to determine benchtop elastic wave velocities. (b) Schematic diagram of the experimental arrangement used for our thermal stressing experiments. (c) Schematic diagram of the experimental arrangement used for our uniaxial compression experiments.

the sample using an electronic balance. After equilibration, water permeability (κ_{water}) could be calculated using Darcy's law:

$$\frac{Q}{A} = \frac{\kappa_{water}}{\eta L}\left(P_{up} - P_{down}\right) \quad \text{(A9)}$$

where Q is the volume of fluid measured per unit time (fluid volume flux), A is the cross-sectional area of the sample, η is the viscosity of the pore fluid, and L is the length of the sample.

A5. Uniaxial Compressive Strength Measurements

Uniaxial compressive strength (UCS) tests were performed on two cylindrical samples (dried in a vacuum oven at 40°C for at least 24 h prior to experimentation) of similar porosity from each of the five blocks of andesite. The experiments were conducted in a uniaxial press (Laboratoire de Déformation des Roches, Strasbourg, see Figure A2) under ambient laboratory conditions (i.e., ambient humidity, room pressure, and temperature) at a constant strain rate of $10^{-5}\,s^{-1}$ until failure. Although such a strain rate exceeds characteristic tectonic strain rates (that are typically on the order of $10^{-14}\,s^{-1}$) [see *Whitten*, 1956; *Wood*, 1973], volcano-tectonic environments, affected by magmatic and eruptive activities, will undoubtedly experience much higher strain rates [*Borgia*, 1994; *Takada*, 1994]. Indeed, this experimental strain rate is equivalent to strain rates observed in lava domes and inferred along the margins of magma conduits [*Rust et al.*, 2003]. Whereas we understand that unconfined compression experiments performed under ambient laboratory conditions may not accurately represent the natural case, this method is nevertheless considered as the "standard" way to assess rock strength [*International Society of Rock Mechanics*, 2007] allowing our data (1) to be compared with the wealth of preexisting data and (2) to be used in micromechanical modeling.

During deformation, axial strain and stress were continuously monitored by an LVDT (linear variable differential transducer) displacement transducer and a load cell, respectively. The output of acoustic emissions (AEs) during deformation was continuously monitored using a piezoelectric AE transducer (WD wideband sensors from Physical Acoustics Corporation) located within the bottom endcap (Figure A2) connected to a PCI-2 MISTRAS AE system (sampling at a rate of 5 MHz). AEs are high-frequency elastic wave packets generated by the rapid release of strain energy such as during brittle microfracturing (see *Lockner* [1993] for a review). During experimentation, an AE hit was recorded if a signal exceeded the set threshold of 30 dB. The amplitude and "energy" (the area under the received AE waveform envelope) of each received AE signal were provided by the AEwin software. Further, the received AE signals were also statistically analyzed using the analogous seismic b value [*Aki*, 1965] to characterize the nature of the microcracking in our samples. The b value describes the slope of the amplitude to frequency distribution of AEs, commonly used to describe the size-frequency distribution of microcracking events in rock deformation experiments [*Meredith and Atkinson*, 1983; *Main et al.*, 1989; *Smith et al.*, 2009; *Sammonds et al.*, 1992].

A6. Thermal Stressing Experiments

The rocks that comprise a volcanic edifice are, as a result of sustained magmatic and hydrothermal activity, subjected to high temperatures (e.g., 300–700°C). Numerical simulations of dyke emplacement highlight the potential for thermal stressing of the host rocks on a scale of several meters [*Carrigan et al.*, 1992], whereas larger bodies (such as magma reservoirs) can generate kilometer-scale thermal aureoles [*Bonaccorso et al.*, 2010]. With the aim of a better understanding of volcanically active provinces, we have assessed the impact of thermal stressing (to 450°C, representative of the temperatures at conduit margins) on the microstructural, physical, and mechanical properties of the andesites. We note that this temperature is within the stability field of the mineralogical assemblage, as well as the brittle limit set by the glass transition [*Lavallée et al.*, 2012]. First, each sample underwent a systematic physical property characterization. Second, each sample was thermally stressed in a high-temperature uniaxial press (at Earth and Environment, LMU, Munich, Figure A2). Samples were placed between the two pistons, and an axial stress of about 3 MPa was applied to the sample (provided simply by the mass of the upper piston). The furnace temperature was then set to climb to 500°C at 1°C/min, hold at 500°C for 60 min, and then cool back to the ambient laboratory temperature at a rate of 1°C/min (Figure 5). This procedure ensured that the sample temperature reached the target of 450°C (measured by an additional thermocouple adjacent to the sample, see Figure A2). We note that the heating

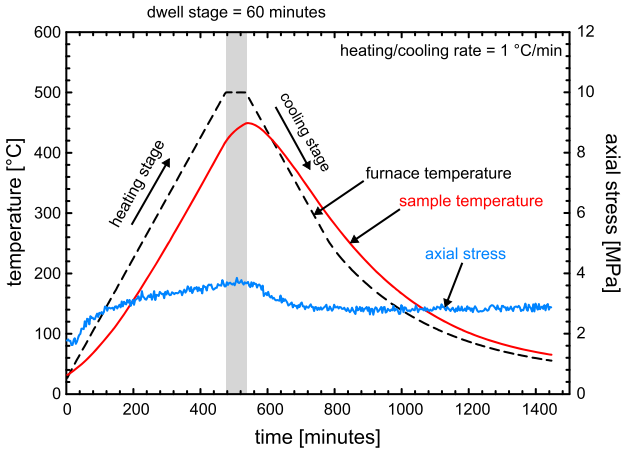

Figure A3. A time-temperature plot outlining the methodology for our thermal stressing experiments.

rate of the sample accurately matched the furnace heating rate (above temperatures of 100°C). However, the sample cooling rate was lower than that of the furnace, and the furnace could not cool at 1°C/min below furnace temperatures of about 250°C (Figure A3). During thermal stressing we continuously recorded the furnace temperature, the temperature adjacent to the sample, axial stress, and the output of AE (to be used as a proxy for the initiation and propagation of thermal microcracks). The generation of thermal microcracks during thermal stressing experiments has been previously monitored using the output AE [e.g., *Meredith et al.*, 1990; *Glover et al.*, 1995; *Jones et al.*, 1997; *Heap et al.*, 2013]. The pistons of the press were used as waveguides for the monitoring of AE using the same AE system described above (although the amplitude threshold was increased to 50 dB to eliminate electrical and background noise). Third, each sample underwent a systematic physical property recharacterization. Fourth, we determined their UCS (again using two samples per rock type). To best compare the mechanical behavior of the "as-collected" (i.e., samples that have undergone no additional heating or deformation) and thermally stressed andesites, we selected core samples that contained similar initial porosities. Finally, thin sections, again in the *XY* plane, of the thermally stressed andesites were prepared for microcrack density and anisotropy analysis.

Acknowledgments

First, we would like to thank Sebastian Mueller and Olivier Spieler for collecting the experimental materials in 2004 (field campaign supported by the R&D Programme GEOTECHNOLOGIEN, funded by the German Ministry of Education and Research (BMBF) and German Research Foundation (DFG), grant PTJ MGS/03G584A-SUNDAARC-DEVACOM). This research was partly funded by the DAAD-CONACYT cooperation program between Germany and Mexico and by the Bavarian Elite Network. Lavallée acknowledges financial support from the DFG grant LA2651/3-1 and ERC starting grant "SLiM" (Strain Localisation in Magmas, project 306488). M. J. Heap, D. B. Dingwell, and Y. Lavallée acknowledge the support of a Hubert Curien Partnership (PHC) PROCOPE grant (grant 27061UE), the Deutscher Akademischer Austauschdienst (DAAD) in Germany, and the Ministry of Foreign and European Affairs (MAE) and the Ministry of Higher Education and Research (MESR), both in France. Dingwell also acknowledges a research professorship from the Bundesexzellenzinitiative (LMUexcellent) and the ERC advanced grant "EVOKES" (Explosive volcanism in the Earth system: experimental insights, project 247076). M. J. Heap also acknowledges CNRS INSU grant "*Étude de la stabilité des édifices volcaniques*." We thank Teng-fong Wong for fruitful discussions and Alan George Heap and Fabian Wadsworth for measuring the powdered skeletal densities. We would like to thank Sebastian Mueller and Agust Gudmundsson for their constructive reviews that greatly improved this manuscript.

References

Adelinet, M., J. Fortin, A. Schubnel, and Y. Guéguen (2013), Deformation modes in an Icelandic basalt: From brittle failure to localized deformation bands, *J. Volcanol. Geotherm. Res.*, *255*, 12–25.

Aki, K. (1965), Maximum likelihood estimate of b in the formula log N = a-bM and its confidence limits, *Bull. Earthquake Res. Inst.*, *43*, 237–239.

Arámbula-Mendoza, R., P. Lesage, C. Valdés-González, N. R. Varley, G. Reyes-Dávila, and C. Navarro (2011), Seismic activity that accompanied the effusive and explosive eruptions during the 2004–2005 period at Volcán de Colima, Mexico, *J. Volcanol. Geotherm. Res.*, *205*, 30–46.

Ashby, M. F., and C. G. Sammis (1990), The damage mechanics of brittle solids in compression, *Pure Appl. Geophys.*, *133*, 489–521.

Balme, M. R., V. Rocchi, C. Jones, P. R. Sammonds, P. G. Meredith, and S. A. Boon (2004), Fracture toughness measurements on igneous rocks using a high-pressure, high-temperature rock fracture mechanics cell, *J. Volcanol. Geotherm. Res.*, *132*, 159–172.

Baud, P., W. Zhu, and T.-F. Wong (2000), Failure mode and weakening effect of water on sandstone, *J. Geophys. Res.*, *105*, 16,371–16,389.

Baud, P., T.-f. Wong, and W. Zhu (2014), Effects of porosity and crack density on the compressive strength of rocks, *Int. J. Rock Mech. Mining Sci.*, *67*, 202–211, doi:10.1016/j.ijrmms.2013.08.031.

Bauer, S. J., M. Friedman, and J. Handin (1981), Effects of water-saturation on strength and ductility of three igneous rocks at effective pressures to 50 MPa and temperatures to partial melting, *The 22nd U.S. Symposium on Rock Mechanics (USRMS)*, June 29–July 2, 1981, Cambridge, Mass.

Benson, P. M., S. Vinciguerra, P. G. Meredith, and R. P. Young (2008), Laboratory simulation of volcano seismicity, *Science*, *322*, 249–252.

Bernabé, Y., U. Mok, and B. Evans (2003), Permeability-porosity relationships in rocks subjected to various evolution processes, *Pure Appl. Geophys.*, *160*, 937–960.

Bernabé, Y., M. Li, and A. Maineult (2010), Permeability and pore connectivity: A new model based on network simulations, *J. Geophys. Res.*, *155*, B10203, doi:10.1023/2010JB007444.

Bernard, M.-L., M. Zomara, Y. Géraud, and G. Boudon (2007), Transport properties of pyroclastic rocks from Montagne Pelée volcano (Martinique, Lesser Antilles), *J. Geophys. Res.*, *112*, B05205, doi:10.1029/2006JB004385.

Blake, O. O., D. R. Faulkner, and A. Reitbrock (2013), The effect of varying damage history in crystalline rocks on the P- and S-wave velocity under hydrostatic confining pressure, *Pure Appl. Geophys.*, *170*, 493–505.

Bonaccorso, A., G. Currenti, C. Del Negro, and E. Boschi (2010), Dike deflection modelling for inferring magma pressure and withdrawal, with application to Etna 2001 case, *Earth Planet. Sci. Lett.*, *293*, 121–129.

Borgia, A. (1994), Dynamic basis of volcanic spreading, *J. Geophys. Res.*, *99*, 17,791–17,804.

Borselli, L., L. Capra, D. Sarocchi, and S. De la Cruz-Reyna (2011), Flank collapse scenarios at Volcán de Colima, Mexico: A relative instability analysis, *J. Volcanol. Geotherm. Res.*, *208*, 51–65.

Bourbié, T., and B. Zinszner (1985), Hydraulic and acoustic properties as a function of porosity in Fontainebleau Sandstone, *J. Geophys. Res.*, *90*, 11,524–11,532.

Brace, W. F., B. W. Paulding, and C. H. Scholz (1966), Dilatancy in the fracture of crystalline rocks, *J. Geophys. Res.*, *71*, 3939–3953.

Caricchi, L., A. Pommier, M. Pistone, J. Castro, A. Burgisser, and D. Perugini (2011), Strain-induced magma degassing: Insights from simple-shear experiments on bubble bearing melts, *Bull. Volcanol.*, *73*, 1245–1257.

Carman, P. (1937), Fluid flow through a granular bed, *Trans. Inst. Chem. Eng.*, *15*, 150–167.

Carrigan, C. R., G. Schubert, and J. C. Eichelberger (1992), Thermal and dynamical regimes of single- and two-phase magmatic flow in dikes, *J. Geophys. Res.*, *97*, 17,377–17,392.

Chang, C., M. D. Zoback, and A. Khaksar (2006), Empirical relations between rock strength and physical properties in sedimentary rocks, *J. Pet. Sci. Eng.*, *51*, 223–237.
Cheng, C. H., and D. H. Johnston (1981), Dynamic and static moduli, *Geophys. Res. Lett.*, *8*, 39–42.
Ciccotti, M., and F. Mulargia (2004), Differences between static and dynamic elastic moduli of a typical seismogenic rock, *Geophys. J. Int.*, *157*, 474–477.
Ciccotti, M., N. Negri, L. Sassi, G. Gonzato, and F. Mulargia (2000), Elastic and fracture parameters of Etna, Stromboli, and Vulcano lava rocks, *J. Volcanol. Geotherm. Res.*, *98*, 209–217.
Cook, N. W. G., (1981), Stiff testing machines, stick slip sliding, and the stability of rock deformation, in *Mechanical Behavior of Crustal Rocks: The Handin Volume*, edited by N. L. Carter et al., pp. 93–102, AGU, Washington, D. C., doi:10.1029/GM024p0093.
Cortés, A., V. H. Garduño, J. L. Macías, C. Navarro-Ochoa, J. C. Komorowski, R. Saucedo, and J. C. Gavilanes (2010), Geologic mapping of the Colima volcanic complex (Mexico) and implications for hazard assessment, *Geol. Soc. Am. Special Pap.*, *464*, 249–264.
Costa, A. (2006), Permeability-porosity relationship: A reexamination of the Kozeny-Carman equation based on a fractal pore-space geometry assumption, *Geophys. Res. Lett.*, *33*, L02318, doi:10.1029/2005GL025134.
Costa, A., R. S. J. Sparks, G. Macedonio, and O. Melnik (2009), Effects of wall-rock elasticity on magma flow in dykes during explosive eruptions, *Earth Planet. Sci. Lett.*, *288*, 455–462.
David, C., B. Mendez, and M. Darot (1999), Influence of stress-induced and thermal cracking on physical properties and microstructure of La Pyrette Granite, *Int. J. Rock Mech. Mining Sci.*, *36*, 433–448.
David, E. C., N. Brantut, A. Schubnel, and R. W. Zimmerman (2011), Sliding crack model for nonlinearity and hysteresis in the uniaxial stress-strain curve of rock, *Int. J. Rock Mech. Mining Sci.*, *52*, 9–17.
Dávila, N., L. Capra, J. C. Gavilanes-Ruiz, N. Varley, G. Norini, and Á. Gómez-Vázquez (2007), Recent lahars at Volcán de Colima (Mexico): Drainage variation and spectral classification, *J. Volcanol. Geotherm. Res.*, *165*, 127–141.
De la Cruz-Reyna, S., and G. A. Reyes-Davila (2001), A model to describe precursory material-failure phenomena: Applications to short-term forecasting at Colima volcano, Mexico, *Bull. Volcanol.*, *63*, 297–308.
Donnadieu, F., O. Merle, and J. C. Besson (2001), Volcanic edifice stability during cryptodome intrusion, *Bull. Volcanol.*, *63*, 61–72.
Doyen, P. M. (1988), Permeability, conductivity, and pore geometry of sandstone, *J. Geophys. Res.*, *93*, 7729–7740.
Dullien, F. A. L. (1979), *Porous Media: Fluid Transport and Pore Structure*, Academic, New York.
Eichelberger, J. C., C. R. Carrigan, H. R. Westrich, and R. H. Price (1986), Non-explosive silicic volcanism, *Nature*, *323*, 598–602.
Eissa, E. A., and A. Kazi (1989), Relation between static and dynamic Young's moduli of rocks, *Int. J. Rock Mech. Mining Sci. Geomechanics Abstr.*, *25*, 479–482.
Fortin, J., S. Stantchits, S. Vinciguerra, and Y. Guéguen (2011), Influence of thermal and mechanical cracks on permeability and elastic wave velocities in a basalt from Mt. Etna volcano subjected to elevated pressure, *Tectonophysics*, *503*, 60–74, doi:10.1016/j.tecto.2010.09.028.
Gerik, A., and J. H. Kruhl (2009), Towards automated pattern quantification: Time-efficient assessment of anisotropy of 2D patterns with AMOCADO, *Comput. Geosci.*, *35*, 1087–1097.
Glover, P. W. J., P. Baud, M. Darot, P. G. Meredith, S. A. Boon, M. LeRevelec, S. Zoussi, and T. Reuschlé (1995), α/β phase transition in quartz monitored using acoustic emissions, *Geophys. J. Int.*, *120*, 775–782.
Gottsmann, J., S. De Angelis, N. Fournier, M. Van Camp, S. Sacks, A. Linde, and M. Ripepe (2011), On the geophysical fingerprint of Vulcanian explosions, *Earth Planet. Sci. Lett.*, *306*, 98–104.
Gudmundsson, A. (2011), *Rock Fractures in Geological Processes*, Cambridge Univ. Press, Cambridge, U. K.
Gudmundsson, A. (2012), Strengths and strain energies of volcanic edifices: Implications for eruptions, collapse calderas, and landslides, *Nat. Hazards Earth Syst. Sci.*, *12*, 2241–2258.
Guéguen, Y., and V. Palciauskas (1994), *Introduction to the Physics of Rocks*, Princeton Univ. Press, Princeton, N. J.
Heap, M. J., and D. R. Faulkner (2008), Quantifying the evolution of static elastic properties as crystalline rock approaches failure, *Int. J. Rock Mech. Mining Sci.*, *45*, 564–573.
Heap, M. J., S. Vinciguerra, and P. G. Meredith (2009), The evolution of elastic moduli with increasing crack damage during cyclic stressing of a basalt from Mt. Etna volcano, *Tectonophysics*, *471*, 153–160.
Heap, M. J., D. R. Faulkner, P. G. Meredith, and S. Vinciguerra (2010), Elastic moduli evolution and accompanying stress changes with increasing crack damage: Implications for stress changes around fault zones and volcanoes during deformation, *Geophys. J. Int.*, *183*, 225–236.
Heap, M. J., P. Baud, P. G. Meredith, S. Vinciguerra, A. F. Bell, and I. G. Main (2011), Brittle creep in basalt and its application to time-dependent volcano deformation, *Earth Planet. Sci. Lett.*, *307*, 71–82.
Heap, M. J., Y. Lavallée, A. Laumann, K.-U. Hess, P. G. Meredith, and D. B. Dingwell (2012), How tough is tuff in the event of fire?, *Geology*, *40*, 311–314.
Heap, M. J., Y. Lavallée, P. G. Meredith, D. B. Dingwell, S. Huismann, and F. Weise (2013), The influence of thermal-stressing (up to 1000 °C) on the physical, mechanical, and chemical properties of siliceous-aggregate, high-strength concrete, *Construction Building Mater.*, *42*, 248–265.
Heap, M. J., P. Baud, P. G. Meredith, S. Vinciguerra, and T. Reuschlé (2014), The permeability and elastic moduli of tuff from Campi Flegrei, Italy: Implications for ground deformation modelling, *Solid Earth*, *5*, 25–44.
Hoek, E., and Z. T. Bieniawski (1965), Brittle fracture propagation in rock under compression, *Int. J. Fract.*, *1*, 137–155.
Homand-Etienne, F., and R. Houpert (1989), Thermally induced microcracking in granite: Characterisation and analysis, *Int. J. Rock Mech. Mining Sci. Geomech. Abstr.*, *26*(2), 125–134.
Horii, H., and S. Nemat-Nasser (1986), Brittle failure in compression: Splitting, faulting and brittle-ductile transition, *Phil. Trans. Royal Soc. London*, *319*, 337–374.
Hutchinson, W., N. Varley, D. M. Pyle, and T. A. Mather (2013), Airborne thermal remote sensing of the Volcán de Colima (Mexico) lava dome from 2007 to 2010, in *Remote Sensing of Volcanoes & Volcanic Processes: Integrating Observation & Modelling*, edited by D. L. Pyle and T. A. Mather, pp. 203–228, Geological Society of London, London, U. K.
International Society of Rock Mechanics (2007), Part 1 - SM for determination of the uniaxial compressive strength of rock materials, in *The Complete ISRM Suggested Methods for Rock Characterization, Testing and Monitoring: 1974–2006*, edited by R. Ulusay and J. A. Hudson, pp. 151–156, IRSM Turkish National Group, Ankara, Turkey.
Jaeger, J., N. G. W. Cook, and R. Zimmerman (2007), *Fundamentals in Rock Mechanics*, 4th ed., Blackwell Publishing, London.
Jaupart, C. (1998), Gas loss from magmas through conduit walls during eruption, *Geol. Soc. London, Special Publ.*, *145*, 73–90.
Jeong, H.-s., S.-s. Kang, and Y. Obara (2007), Influence of surrounding environments and strain rates on the strength of rocks subjected to uniaxial compression, *Int. J. Rock Mech. Mining Sci.*, *44*, 321–331.

Jones, C., G. Keaney, P. G. Meredith, and S. A. F. Murrell (1997), Acoustic emission and fluid permeability measurements on thermally cracked rocks, *Phys. Chem. Earth*, *22*(1-2), 13–17.
Keles, C., and L. Tutluoglu (2011), Investigation of proper specimen geometry for mode I fracture toughness testing with flattened Brazilian disc method, *Int. J. Fract.*, *169*, 61–75.
Kemeny, J. M., and N. W. G. Cook (1991), Micromechanics of deformation in rocks, in *Toughening Mechanisms in Quasi-Brittle Materials*, edited by S. P. Shah, pp. 155–188, Kluwer Academic Publishers, Dordrecht, Netherlands.
Kendrick, J. E., Y. Lavallée, K.-U. Hess, M. J. Heap, H. E. Gaunt, P. G. Meredith, and D. B. Dingwell (2013), Tracking the permeable porous network during strain-dependent magmatic flow, *J. Volcanol. Geotherm. Res.*, *260*, 117–126.
Kilburn, C. R. J. (2003), Multiscale fracturing as a key to forecasting volcanic eruptions, *J. Volcanol. Geotherm. Res.*, *125*, 271–289.
Kilburn, C. R. J., and P. R. Sammonds (2005), Maximum warning times for imminent volcanic eruptions, *Geophys. Res. Lett.*, *32*, L24313, doi:10.1029/2005GL024184.
Kirchhoff, G., W. Pompe, and H.-A. Bahr (1982), Structure dependence of thermally induced microcracking in porcelain studied by acoustic emission, *J. Mater. Sci.*, *17*, 2809–2816.
Klug, C., and K. V. Cashman (1996), Permeability development in vesiculating magmas: Implications for fragmentation, *Bull. Volcanol.*, *58*, 87–100.
Kolzenburg, S., M. J. Heap, Y. Lavallée, J. K. R. Russell, P. G. Meredith, and D. B. Dingwell (2012), Strength and permeability recovery of tuffisite-bearing andesite, *Solid Earth*, *3*, 191–198.
Kozeny, J. (1927), Ueber kapillare Leitung der Wasser in Boden, *Sitzungsber. Akad. Wiss. Wien*, *136*, 271–306.
Laumonier, M., L. Arbaret, A. Burgisser, and R. Champallier (2011), Porosity redistribution enhanced by strain localisation in crystal-rich magmas, *Geology*, *39*, 715–718.
Lavallée, Y., P. G. Meredith, D. B. Dingwell, K. U. Hess, J. Wassermann, B. Cordonnier, A. Gerik, and J. H. Kruhl (2008), Seismogenic lavas and explosive eruption forecasting, *Nature*, *453*, 507–510.
Lavallée, Y., N. Varley, M. A. Alatorre-Ibargüengoitia, K.-U. Hess, U. Kueppers, S. Mueller, D. Richard, B. Scheu, O. Spieler, and D. B. Dingwell (2012), Magmatic architecture of dome-building eruptions at Volcán de Colima, Mexico, *Bull. Volcanol.*, *74*, 249–260.
Lavallée, Y., P. M. Benson, M. J. Heap, K.-U. Hess, A. Flaws, B. Schillinger, P. G. Meredith, and D. B. Dingwell (2013), Reconstructing magma failure and the degassing network of dome-building eruptions, *Geology*, *41*, 515–518.
Lebedev, E. B., and H. Kern (1999), The effect of hydration and dehydration reactions on wave velocities in basalts, *Tectonophysics*, *308*, 331–340.
Loaiza, S., J. Fortin, A. Schubnel, Y. Guéguen, S. Vinciguerra, and M. Moreira (2012), Mechanical behavior and localized failure modes in a porous basalt from the Azores, *Geophys. Res. Lett.*, *39*, L19304, doi:10.1029/2012GL053218.
Lockner, D. (1993), The role of acoustic emission in the study of rock fracture, *Int. J. Rock Mech. Mining Sci. Geomech. Abstr.*, *30*, 883–889.
Luhr, J. F. (2002), Petrology and geochemistry of the 1991 and 1998–1999 lava flows from Volcán de Colima, México: Implications for the end of the current eruptive cycle, *J. Volcanol. Geotherm. Res.*, *117*, 169–194.
Main, I. G., P. G. Meredith, and C. Jones (1989), A reinterpretation of the precursory seismic b-value anomaly from fracture-mechanics, *Geophys. J. Oxford*, *96*, 131–138.
Manconi, A., T. R. Walter, and F. Amelung (2007), Effects of mechanical layering on volcano deformation, *Geophys. J. Int.*, *170*, 952–958.
Manconi, A., T. R. Walter, M. Manzo, G. Zeni, P. Tizzani, E. Sansosti, and R. Lanari (2010), On the effects of 3D mechanical heterogeneities at Campi Flegrei caldera, southern Italy, *J. Geophys. Res.*, *115*, B08405, doi:10.1029/2009JB007099.
McGuire, W. J. (1996), Volcano instability: A review of contemporary themes, *Geol. Soc. London*, *110*, 1–23.
Meredith, P. G., and B. K. Atkinson (1983), Stress corrosion and acoustic emission during tensile crack propagation in Whin Sill dolerite and other basic rocks, *Geophys. J. R. Astron. Soc.*, *75*, 1–21.
Meredith, P. G., I. G. Main, and C. Jones (1990), Temporal variations in seismicity during quasi-static and dynamic rock failure, *Tectonophysics*, *175*, 249–268.
Meredith, P. G., O. Lewis, S. Vinciguerra, C. Trovato, and P. M. Benson (2005), The influence of microcracks on the physical and mechanical properties of Etna and Iceland basalt, Abstract #V24B-08 presented at 2005 Fall Meeting, AGU, San Francisco, Calif.
Mueller, S. B., N. R. Varley, U. Kueppers, P. Lesage, G. Á. Reyes Davila, and D. B. Dingwell (2013), Quantification of magma ascent rate through rockfall monitoring at the growing/collapsing lava dome of Volcán de Colima, Mexico, *Solid Earth*, *4*, 201–213.
Mueller, S. P. (2006), Permeability and porosity as constraints on the explosive eruption of magma: Laboratory experiments and field investigations, PhD thesis, University of Munich, Munich, Germany.
Mueller, S., O. Melnik, O. Spieler, B. Scheu, and D. B. Dingwell (2005), Permeability and degassing of dome lavas undergoing rapid decompression: An experimental study, *Bull. Volcanol.*, *67*, 526–538.
Mueller, S., B. Scheu, O. Spieler, and D. B. Dingwell (2008), Permeability control on magma fragmentation, *Geology*, *36*, 399–402.
Murray, J. B., and J. J. Ramírez Ruiz (2002), Long-term predictions of the time of eruptions using remote distance measurement at Volcán de Colima, México, *J. Volcanol. Geotherm. Res.*, *117*, 79–89.
Murray, J. B., and L. K. Wooller (2002), Persistent summit subsidence at Volcan de Colima, Mexico,1982–1999: Strong evidence against Mogi deflation, *J. Volcanol. Geotherm. Res.*, *117*, 69–78.
Nara, Y., P. G. Meredith, T. Yoneda, and K. Kaneko (2011), Influence of macro-fractures and micro-fractures on permeability and elastic wave velocities in basalt at elevated pressure, *Tectonophysics*, *503*, 52–59.
Nara, Y., K. Morimoto, N. Hiroyoshi, T. Yoneda, K. Kaneko, and P. M. Benson (2012), Influence of relative humidity on fracture toughness of rock: Implications for subcritical crack growth, *Int. J. Solids Struct.*, *49*, 2471–2481.
Norini, G., L. Capra, G. Groppelli, F. Agliardi, A. Pola, and A. Cortés (2010), Structural architecture of the Colima Volcanic Complex, *J. Geophys. Res.*, *115*, B12209, doi:10.1029/2010JB007649.
Obara, Y., K. Sakaguchi, T. Nakayama, and K. Sugawara (1992), Anisotropy effect on fracture toughness of rock, in *ISRM Symposium Eurock 1992 "Rock Characterisation"*, edited by J. A. Hudson, pp. 7–12, British Geotechnical Society, London, U. K.
O'Connell, R. J., and B. Budiansky (1974), Seismic velocities in dry and saturated cracked solids, *J. Geophys. Res.*, *79*, 5412–5426.
Ouchterlony, F. (1990), Fracture toughness testing or rock with core based specimens, *Eng. Fracture Mech.*, *35*, 351–366.
Paterson, M. S. (1983), The equivalent channel model for permeability and resistivity in fluid-saturated rock - A re-appraisal, *Mech. Mater.*, *2*, 345–352.
Paterson, M. S., and T.-F. Wong (2005), *Experimental Rock Deformation: The Brittle Field*, Springer, New York.
Pinel, V., A. Hooper, S. De la Cruz-Reyna, G. A. Reyes-Davila, M. P. Doin, and P. Bascou (2011), The challenging retrieval of the displacement field from InSAR data for andesitic stratovolcanoes: Case study of Popocatepetl and Colima Volcano, Mexico, *J. Volcanol. Geotherm. Res.*, *200*, 49–61.

Plail, M., M. Edmonds, C. S. Humphreys, J. Barclay, and R. A. Herd (2014), Geochemical evidence for relict degassing pathways preserved in andesite, *Earth Planet. Sci. Lett.*, *386*, 21–33.
Reubi, O., and J. Blundy (2008), Assimilation of plutonic roots, formation of high-K exotic melt inclusions and genesis of andesitic magmas at Volcan De Colima, Mexico, *J. Petrol.*, *49*, 2221–2243.
Reubi, O., J. Blundy, and N. R. Varley (2013), Volatiles contents, degassing and crystallisation of intermediate magmas at Volcan de Colima, Mexico, inferred from melt inclusions, *Contrib. Mineral. Petrol.*, *165*, 1087–1106.
Richard, D., B. Scheu, S. P. Mueller, O. Spieler, and D. B. Dingwell (2013), Outgassing: Influence on speed of magma fragmentation, *J. Geophys. Res. Solid Earth*, *118*, 862–877, doi:10.1002/jgrb.50080.
Richter, D., and G. Simmons (1974), Thermal expansion behaviour of igneous rocks, *Int. J. Rock Mech. Mining Sci.*, *11*, 403–411.
Rocchi, V., P. R. Sammonds, and C. R. J. Kilburn (2004), Fracturing of Etnean and Vesuvian rocks at high temperatures and low pressures, *J. Volcanol. Geotherm. Res.*, *132*, 137–157.
Rust, A. C., M. Manga, and K. V. Cashman (2003), Determining flow type, shear rate and shear stress in magmas from bubble shapes and orientations, *J. Volcanol. Geotherm. Res.*, *122*, 111–132.
Rust, A., and K. V. Cashman (2004), Permeability of vesicular silicic magma: Inertial and hysteresis effects, *Earth Planet. Sci. Lett.*, *228*, 93–107.
Rutter, E. (1986), On the nomenclature of mode of failure transitions in rocks, *Tectonophysics*, *122*, 381–387.
Saar, M. O., and M. Manga (1999), Permeability-porosity relationship in vesicular basalts, *Geophys. Res. Lett.*, *26*, 111–114.
Sammis, C. G., and M. F. Ashby (1986), The failure of brittle porous solids under compressive stress states, *Acta. Metall.*, *34*, 511–526, doi:10.1016/0001-6160(86)90087-8.
Sammonds, P. R., P. G. Meredith, and I. G. Main (1992), Role of pore fluids in the generation of seismic precursors to shear fracture, *Nature*, *359*, 228–230.
Saucedo, R., J. L. Macías, J. C. Gavilanes, J. L. Arce, J. C. Komorowski, J. E. Gardner, and G. Valdez-Moreno (2010), Eyewitness, stratigraphy, chemistry, and eruptive dynamics of the 1913 Plinian eruption of Volcán de Colima, México, *J. Volcanol. Geotherm. Res.*, *191*, 149–166.
Savov, I. P., J. F. Luhr, and C. Navarro-Ochoa (2008), Petrology and geochemistry of lava and ash erupted from Volcán Colima, Mexico, during 1998–2005, *J. Volcanol. Geotherm. Res.*, *174*, 241–256.
Scholz, C. H. (1968), Microfracturing and the inelastic deformation of rock in compression, *J. Geophys. Res.*, *73*, 1417–1432.
Schubnel, A., P. M. Benson, B. D. Thompson, J. Hazzard, and R. P. Young (2006), Quantifying damage, saturation and anisotropy in cracked rocks by inverting elastic wave velocities, *Pure Appl. Geophys.*, *163*, 947–973.
Shea, T., B. F. Houghton, L. Gurioli, K. V. Cashman, J. E. Hammer, and B. J. Hobden (2010), Textural studies of vesicles in volcanic rocks: An integrated methodology, *J. Volcanol. Geotherm. Res.*, *190*, 271–289.
Simmons, G., and W. F. Brace (1965), Comparison of static and dynamic measurements of compressibility of rocks, *J. Geophys. Res.*, *70*, 5649–5656.
Smith, R., P. R. Sammonds, and C. R. J. Kilburn (2009), Fracturing of volcanic systems: Experimental insights into pre-eruptive conditions, *Earth Planet. Sci. Lett.*, *280*, 211–219.
Smith, R., P. Sammonds, H. Tuffen, and P. G. Meredith (2011), Evolution of the mechanics of the 2004–2008 Mt. St. Helens lava dome with time and temperature, *Earth Planet. Sci. Lett.*, *307*, 191–200.
Sparks, R. S. J. (2003), Forecasting volcanic eruptions, *Earth Planet. Sci. Lett.*, *210*, 1–15.
Spieler, O., B. Kennedy, U. Kueppers, D. B. Dingwell, B. Scheu, and J. Taddeucci (2004), The fragmentation threshold of pyroclastic rocks, *Earth Planet. Sci. Lett.*, *226*, 139–148.
Stanchits, S., S. Vinciguerra, and G. Dresen (2006), Ultrasonic velocities, acoustic emission characteristics and crack damage of basalt and granite, *Pure Appl. Geophys.*, *163*, 975–994.
Stasiuk, M. V., J. Barclay, M. R. Carroll, C. Jaupart, J. C. Ratté, R. S. J. Sparks, and S. R. Tait (1996), Degassing during magma ascent in the Mule Creek vent (USA), *Bull. Volcanol.*, *58*, 117–130.
Stevenson, J. A., and N. Varley (2008), Fumarole monitoring with a handheld infrared camera: Volcán de Colima, Mexico, 2006–2007, *J. Volcanol. Geotherm. Res.*, *177*, 911–924.
Sulpizio, R., L. Capra, D. Sarocchi, R. Saucedo, J. C. Gavilanes-Ruiz, and N. R. Varley (2010), Predicting the block-and-ash flow inundation areas at Volcán de Colima (Colima, Mexico) based on the present day (February 2010) status, *J. Volcanol. Geotherm. Res.*, *193*, 49–66.
Takada, A. (1994), The influence of regional stress and magmatic input on styles of monogenetic and polygenetic volcanism, *J. Volcanol. Geotherm. Res.*, *99*, 13,563–13,573.
Tang, S. B., C. A. Tang, Z. Z. Liang, and Y. F. Zhang (2011), Influence of heterogeneity on strength and failure characterization of cement-based composite subjected to uniform thermal loading, *Constr. Build. Mater.*, *25*, 3382–3392.
Taran, Y., J. C. Gavilanes, and A. Cortés (2002), Chemical and isotopic composition of fumarolic gases and the SO2 flux from Volcán de Colima, Mexico, between the 1994 and 1998 eruptions, *J. Volcanol. Geotherm. Res.*, *117*, 105–119.
Tribaudino, M., R. J. Angel, F. Cámara, F. Nestola, D. Pasqual, and I. Margiolaki (2010), Thermal expansion of plagioclase feldspars, *Contrib. Mineral. Petrol.*, *160*, 899–908.
Tuffen, H., D. B. Dingwell, and H. Pinkerton (2003), Repeated fracture and healing of silicic magma generate flow banding and earthquakes?, *Geology*, *31*, 1089–1092.
Underwood, E. E. (1970), *Quantitative Stereology*, Addison Wesley, Reading, Mass.
Vajdova, V., W. Zhu, T.-M. N. Chen, and T.-F. Wong (2010), Micromechanics of brittle faulting and cataclastic flow in Tavel limestone, *J. Struct. Geol.*, *32*, 1158–1169.
Vajdova, V., P. Baud, L. Wu, and T.-f. Wong (2012), Micromechanics of inelastic compaction in two allochemical limestones, *J. Struct. Geol.*, *43*, 100–117.
Varley, N. R., and Y. A. Taran (2003), Degassing processes of Popocatépetl and Volcán de Colima, Mexico, in *Volcanic Degassing*, edited by C. Oppenheimer, D. M. Pyle, and J. Barclay, pp. 263–280, Geological Society of London, London, U. K.
Varley, N., R. Arámbula-Mendoza, G. Reyes-Dávila, J. Stevenson, and R. Harwood (2010), Long-period seismicity during magma movement at Volcán de Colima, *Bull. Volcanol.*, *72*, 1093–1107.
Vasseur, J., F. B. Wadsworth, Y. Lavallée, K.-U. Hess, and D. B. Dingwell (2013), Volcanic sintering: Timescales of viscous densification and strength recovery, *Geophys. Res. Lett.*, *40*, 5658–5664, doi:10.1002/2013GL058105.
Vinciguerra, S., C. Trovato, P. G. Meredith, and P. M. Benson (2005), Relating seismic velocities, thermal cracking and permeability in Mt. Etna and Iceland basalts, *Int. J. Rock Mech. Mining Sci.*, *42*, 900–910.
Voight, B. (1989), A relation to describe rate-dependent material failure, *Science*, *243*, 200–203.
Voight, B. (2000), Structural stability of andesite volcanoes and lava domes, *Philos. Trans. Math. Phys. Eng. Sci.*, *358*(1770), Causes and Consequences of Eruptions of Andesite Volcanoes (May 15, 2000), 1663–1703.

Volland, S., and J. H. Kruhl (2004), Anisotropy quantification: The application of fractal geometry methods on tectonic fracture patterns of a Hercynian fault zone in NW Sardinia, *J. Struct. Geol.*, *26*, 1499–1510.
Walker, G. P. L. (1989), Spongy pahoehoe in Hawaii: A study of vesicle-distribution patterns in basalt and their significance, *Bull. Volcanol.*, *51*, 199–209.
Walsh, J. B., and W. F. Brace (1984), The effect of pressure on porosity and the transport properties of rock, *J. Geophys. Res.*, *89*, 9425–9431.
Whitten, C. A. (1956), Crustal movements in California and Nevada, *Trans. AGU*, *37*, 393–398.
Wong, T.-f. (1985), Geometric probability approach to the characterization and analysis of microcracking in rocks, *Mech. Mater.*, *4*, 261–276.
Wong, T.-f., and P. Baud (2012), The brittle transition in rocks: A review, *J. Struct. Geol.*, *44*, 25–53.
Wood, D. S. (1973), Patterns and magnitudes of natural strain in rocks, *Phil. Trans. R. Soc. London*, *274*, 373–382.
Woods, A. W., and T. Koyaguchi (1994), Transitions between explosive and effusive eruptions of silicic magmas, *Nature*, *370*, 641–644.
Wright, H. M. N., and K. V. Cashman (2013), Compaction and gas loss in welded pyroclastic deposits: Evolution of porosity and permeability in the Shevlin Park Tuff, *Geol. Soc. Am. Bull.*, *126*, 234–247, doi:10.1130/B30668.1.
Wright, H. M. N., J. J. Roberts, and K. V. Cashman (2006), Permeability of anisotropic tube pumice: Model calculations and measurements, *Geophys. Res. Lett.*, *33*, L17316, doi:10.1029/2006GL027224.
Wright, H. M. N., K. V. Cashman, E. H. Gottesfeld, and J. J. Roberts (2009), Pore structure of volcanic clasts: Measurements of permeability and electrical conductivity, *Earth Planet. Sci. Lett.*, *280*, 93–104.
Wu, X. Y., P. Baud, and T.-F. Wong (2000), Micromechanics of compressive failure and spatial evolution of anisotropic damage in Darley Dale sandstone, *Int. J. Rock Mech. Mining Sci.*, *37*, 143–160.
Yokoyama, T., and S. Takeuchi (2009), Porosimetry of vesicular volcanic products by a water-expulsion method and the relationship of pore characteristics to permeability, *J. Geophys. Res.*, *114*, B02201, doi:10.1029/2008JB005758.
Yong, C., and C.-Y. Wang (1980), Thermally induced acoustic emission in Westerly granite, *Geophys. Res. Lett.*, *7*(12), 1089–1092.
Zhu, W., P. Baud, and T.-f. Wong (2010), Micromechanics of cataclastic pore collapse in limestone, *J. Geophys. Res.*, *115*, B04405, doi:10.1029/2009JB006610.
Zhu, W., P. Baud, S. Vinciguerra, and T.-F. Wong (2011), Micromechanics of brittle faulting and cataclastic flow in Alban Hills tuff, *J. Geophys. Res.*, *116*, B06209, doi:10.1029/2010JB008046.
Zoback, M. D. (2010), *Reservoir Geomechanics*, Cambridge Univ. Press, Cambridge, U. K.
Zobin, V. M., M. González-Amezcua, and G. A. Reyes-Dávila (2002a), Seismotectonic deformation of the volcanic edifice prior to the 1998 lava eruption of Volcán de Colima, México, *Bull. Volcanol.*, *64*, 349–355.
Zobin, V. M., M. Gonzalez Amezcua, G. A. Reyes Davila, T. Dominguez, J. C. Cerda Chacon, and J. M. Chavez Alvarez (2002b), Comparative characteristics of the 1997-1998 seismic swarms preceding the November 1998 eruption of Volcan de Colima, Mexico, *J. Volcanol. Geotherm. Res.*, *117*, 47–60.